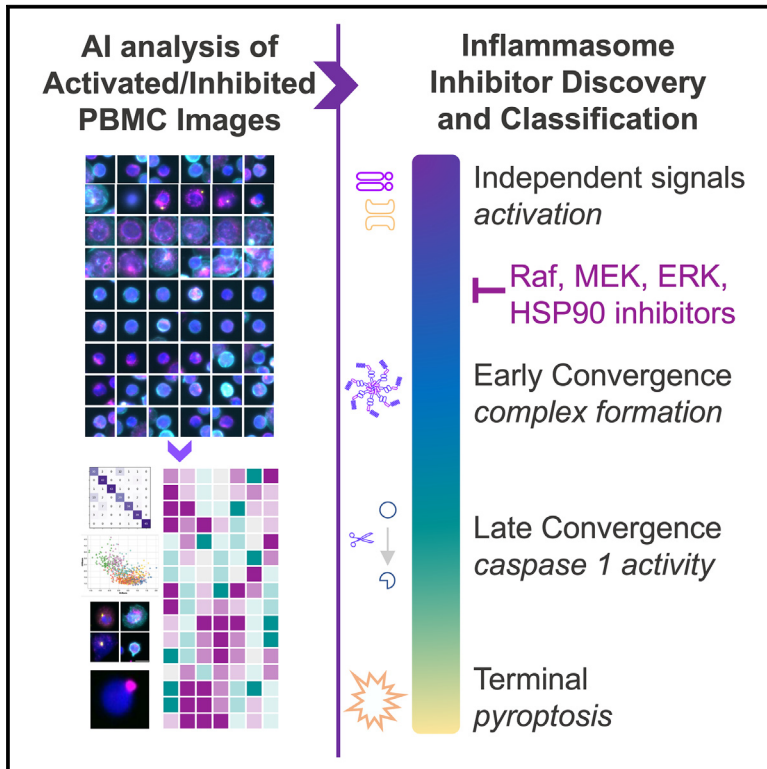# A combined AI and cell biology approach surfaces targets and mechanistically distinct Inflammasome inhibitors

Graphical abstract

Authors

Daniel Chen, Tempest Plott, Michael Wiest, ..., Christian Elabd, Francesco Rubbo, Rachel DeVay Jacobson

Correspondence

rubbo.francesco@gmail.com (F.R.), rachelmarie804@gmail.com (R.D.J.)

In brief

Cell biology; Data analysis; Machine learning

Highlights

- Inflammasomes are linked to a spectrum of acute and chronic human conditions

- Therapeutic development would benefit from being aligned with disease variability

- Machine learning methods resolved a spectrum of inflammasome cellular states

- Surfaced and validated panel of Raf-pathway modulators as inflammasome inhibitors

CellPress

Article

A combined AI and cell biology approach surfaces targets and mechanistically distinct Inflammasome inhibitors

Daniel Chen,[1] Tempest Plott,[1] Michael Wiest,[1] Will Van Trump,[1] Ben Komalo,[1] Dat Nguyen,[1,2] Charlie Marsh,[1,3] Jarred Heinrich,[1,4] Colin J. Fuller,[1] Lauren Nicolaisen,[1,5] Elisa Cambronero,[1,6] An Nguyen,[1] Christian Elabd,[1,7] Francesco Rubbo,[1,8,9,*] and Rachel DeVay Jacobson[1,9,10,*]

[1]Spring Discovery, Inc., 1125 Industrial Road, San Carlos, CA 94070, USA
[2]Present address: Insitro; South San Francisco, CA, United States
[3]Present address: Astral; NY, NY, United States
[4]Present address: Disney Streaming; Los Angeles, CA, United States
[5]Present address: DeepMind; London, United Kingdom
[6]Present address: Gilead Sciences, Foster City, CA, United States
[7]Present address: Stately Bio; San Carlos, CA, United States
[8]Present address: Altos Labs; Redwood Shores, CA, United States
[9]These authors contributed equally
[10]Lead contact
*Correspondence: rubbo.francesco@gmail.com (F.R.), rachelmarie804@gmail.com (R.D.J.)
https://doi.org/10.1016/j.isci.2024.111404

SUMMARY

Inflammasomes are protein complexes that mediate innate immune responses whose dysregulation has been linked to a spectrum of acute and chronic human conditions, which dictates therapeutic development that is aligned with disease variability. We designed a scalable, physiologic high-content imaging assay in human PBMCs that we analyzed using a combination of machine-learning and cell biology methods. This resulted in a set of biologically interpretable readouts that can resolve a spectrum of cellular states associated with inflammasome activation and inhibition. These methods were applied to a phenotypic screen that surfaced mechanistically distinct inflammasome inhibitors from an annotated 12,000 compound library. A set of over 100 inhibitors, including an array of Raf-pathway inhibitors, were validated in downstream functional assays. This approach demonstrates how complementary machine learning-based methods can be used to generate profiles of cellular states associated with different stages of complex biological pathways and yield compound and target discovery.

INTRODUCTION

The innate immune system is our first line of defense against foreign and internal threats, and inflammasome signaling pathways are critical for receiving and amplifying responses to these threats. As such, dysregulation of these pathways has been causally linked to myriad chronic (rheumatoid arthritis,[1] gout[2]) and acute (sepsis,[3] acute respiratory distress syndrome [ARDS[4]]) human inflammatory pathologies, creating need for therapeutic development that is aligned with the diversity of inflammasome-associated human conditions.

Canonical inflammasome pathways are activated through a variety of stimuli, including the danger associated-signal ATP and the pathogen-associated signal flagellin. These primary signals can drive secondary inflammatory responses in neighboring cells by inducing pyroptotic release of inflammatory cytokines and danger associated molecular pattern (DAMP)-containing proteins.[5–7] Inflammasome pathways converge at three stages: (1) expression of pro-IL-1β and pro-IL-18, (2) inflammasome

complex assembly (consists of an NLR/sensor protein, an apoptosis-associated-speck-like protein-containing-a-CARD domain (ASC) protein, and caspase-1), which mediates cleavage of pro-IL-1β, pro-IL-18, and the pore-forming protein Gasdermin D (GSDMD), and (3) GSDMD mediated cellular release of IL-1β, IL-18, and DAMPs, which serves as the terminal step in the inflammasome-mediated cell death process, termed pyroptosis[8–10] (Figure 1A).

Experimentally measuring inflammasome activation and inhibition typically relies on single, late pathway readouts from monocyte-based in vitro systems. As we demonstrate here, these methods are generally unable to resolve the complexities and redundancies of inflammasome signaling, and we therefore expanded on the principles of Cell Painting[11] to develop an in vitro imaging based system coupled with a holistic machine learning (ML) approach to resolve intra- and inter-inflammasome pathway differences in PBMCs for the purpose of discovering multiple, functionally diverse inflammasome inhibitors.
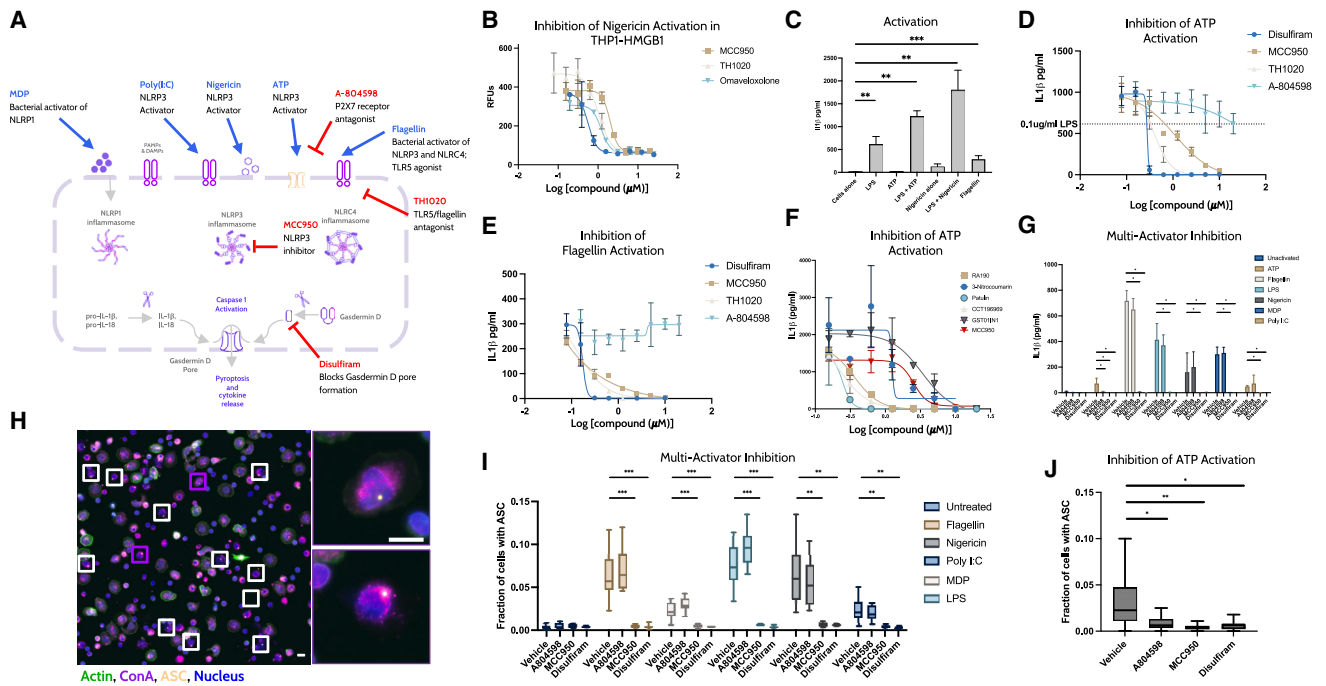
Figure 1. Using conventional monocytic pyroptosis assays to gauge inflammasome inhibition and establishment of a high-content imaging based inflammasome assay in human PBMCs

(A) Schematic of inflammasome pathways, control activators, and inhibitors.

(B) THP-1:HMGB1 Lucia reporter assay stimulated Nigericin following LPS priming. Inflammasome activation and inhibition is measured from extracellular luminescence signal of released HMGB1:Lucia. Signal shown is the average of triplicate points with standard deviation, Z score normalized, and plotted against the log of compound concentration. Curves were fit with a log(agonist) vs. response variable slope (four parameters) least squares fit model.

(C) Primary human monocytes were treated with flagellin alone or ATP and Nigericin with and without an LPS priming step. Inflammasome activation was assessed by extracellular IL-1β levels and compared to vehicle (DMSO) control. Data are shown as the average of four replicates with standard deviation. Statistical significance measured by two-tailed unpaired Mann Whitney U tests; *$p < 0.05$, **$p < 0.005$, ***$p < 0.0005$, (D) Inhibition of ATP-induced inflammasome activation on primary human monocytes with four control compounds: MCC950, TH1020, Disulfiram, and A-804598. Data are shown as average pg/ml IL-1β of triplicates and standard deviation from a representative experiment and fit with a log(agonist) vs. response variable slope (four parameters) least squares fit model.

(E) Inhibition of Flagellin-induced inflammasome activation on primary human monocytes with four control compounds: MCC950, TH1020, Disulfiram, and A-804598. Data are shown as average pg/ml IL-1β of triplicates and standard deviation from a representative experiment and fit with a log(agonist) vs. response variable slope (four parameters) least squares fit model.

(F) Primary human monocytes activated with ATP following LPS priming were inhibited with a set of mechanistically distinct compounds showing different degrees of inhibition. Data are shown as average pg/ml IL-1β of triplicates and standard deviation from a representative experiment and fit with a log(agonist) vs. response variable slope (four parameters) least squares fit model.

(G) Inflammasome activation of human PBMCs with 6 inflammasome stimuli and subsequent inhibition by 20 μM MCC950, 20 μM A-804598, and 40 μM disulfiram. Data shown as average of four replicates from a representative experiment with standard deviation. Statistical significance determined using two-tailed unpaired Mann Whitney U tests; *$p < 0.05$, **$p < 0.005$, ***$p < 0.0005$.

(H) Activated PBMCs stained with cell biological stains: Nucleus (Hoechst; blue), Cell membranes (Concanavalin A; purple), actin cytoskeleton (Phalloidin; green), and ASC (Indirect immunofluorescence of an anti-ASC antibody; yellow). Automated measurements of ASC assess speck presence, area, and cellular distribution. Insets show zoomed in cells with ASC specks. Scale bars for field level image and insets = 10 μm.

(I) ASC speck presence quantification of PBMCs stimulated with LPS, Nigericin, Flagellin, Poly I:C, or MDP. Data are shown as box (median, Q1, Q3) and whiskers (range) of single-well replicates from 12 unique human donors from a representative experiment. Activated PBMCs were inhibited with 3 control inhibitors: MCC950 (20 μM), Disulfiram (40 μM), and A-804598 (20 μM). Statistical significance determined using two-tailed unpaired Mann Whitney U-test; *$p < 0.05$, **$p < 0.005$, ***$p < 0.0005$.

(J) ASC speck presence quantification of ATP activated PBMCs. Data are shown as box (median, Q1, Q3) and whiskers (range) of single replicates from 12 unique human donors from a representative experiment. Activated PBMCs were inhibited with 3 control inhibitors: MCC950 (1 μM), Disulfiram (5 μM), and A-804598 (1 μM). Statistical significance determined using unpaired Mann Whitney U-test; *$p < 0.05$, **$p < 0.005$, ***$p < 0.0005$. See also Figure S1.

To identify and define cellular states that fall along a spectrum from basal to pyroptotic, we first applied supervised and unsupervised ML based methods to high-content imaging data. Interpretable biological metrics were extracted from these methods and validated using established ground-truth measurements across known inflammasome control conditions. These metrics were applied to compound screening data and used to surface a set of mechanistically distinct inhibitors that act at various stages of inflammasome signaling along a spectrum from basal to pyroptotic. From this work, multiple members of the Raf pathway were identified as potent inflammasome targets. Generally, this approach could be used to disambiguate other

interconnected biological pathways (e.g., Wnt or TLR signaling) from high-content imaging data for the purpose of target discovery and drug screening.

RESULTS

Conventional monocytic assays cannot resolve critical intra- or inter-inflammasome pathway differences

We first tested the ability of a commonly used THP1 reporter assay to resolve differences between mechanistically distinct inflammasome pathway inhibitors. In this assay, inflammasome signaling is measured by luminescence detection of pyroptotically released HMGB1:Lucia from cells that are primed using lipopolysaccharide and activated through the NOD-like protein NLRP3 with Nigericin. We tested the system using the control NLRP3 inhibitor MCC950, which mediated an expected dose-dependent inhibition of pyroptosis. We then applied three functionally different compounds, NFkB-in-1 (NFkB inhibitor), TH1020 (TLR5 inhibitor), and omaveloxolone (NRF2 modulator), which all performed similarly to MCC950, despite their unique mechanisms of action (Figure 1B).

We next established a similar system in primary human monocytes to study inflammasome pathways in a more sensitive and physiologically relevant assay. Cells were activated across a series of stimuli and secreted IL-1β was used as a readout of inflammasome activation.[12] LPS priming was required for significant nigericin or ATP mediated IL-1β release through NLRP3, and the NLRC4 activator flagellin induced significant levels of IL-1β release on its own (Figure 1C).

Focusing on two inflammasome activators, we tested the ability of several inflammasome inhibitors to inhibit IL-1β release in monocytes following flagellin or ATP activation. MCC950[13] dose-dependently blocked ATP activation as expected, but it surprisingly also inhibited flagellin mediated IL-1β release despite literature reports indicating flagellin operates through NLRC4.[14] MCC950 may therefore act on NLRP3 that is activated either directly by flagellin[15] or alternatively by pyroptotically released ROS, potassium, or other DAMPs following primary signaling through NLRC4[13,16] in neighboring cells. The gasdermin D inhibitor disulfiram[12] also prevented IL-1β release for both activators, which is expected given its critical role at the terminal stage of convergent inflammasome pathways (Figures 1C–1E), while the ATP receptor P2X7 inhibitor, A-804598, demonstrated expected specificity for ATP activated cells. We hypothesized that TH1020 would show specificity for flagellin activated cells given its reported role as a TLR5 inhibitor, but it potently inhibited pyroptosis in both flagellin and ATP activated cells (Figures 1D and 1E), suggesting it may act promiscuously across inflammasome pathways.

Interestingly, the apoptosis inducers RA190 (proteasome inhibitor) and patulin (mycotoxin) have roughly 10-fold lower IC50s than MCC950 in primary monocytes (Figure 1F), but they likely prevent IL-1β release by shifting to different death programs rather than through direct inhibition of pyroptosis. Thus, these monocytic models measure the potency of inflammasome inhibition, but they are unable to discriminate between mechanistically distinct inhibitors, including those that act non-specifically to bypass inflammasome activation. We therefore set out to establish a physiologically relevant *in vitro* system optimized to discover and characterize mechanistically distinct, inflammasome specific modulators.

Inflammasome activation under various stimulation conditions can be measured from high-content images of primary human PBMCs

We next established a high-content imaging assay of inflammasome activation in primary human peripheral blood mononuclear cells (PBMC). All conditions tested were validated using control inflammasome inhibitors and the established functional readouts IL-1β release and ASC speck presence. These importantly served as ground-truth measurements to validate experimental parameters and downstream machine-learning generated readouts. Additionally, all experiments throughout this study were designed to minimize experimental and biological variability as detailed in the methods and Figure S2.

PBMCs were seeded on 384-well imaging plates and independently activated with MDP, flagellin, Poly I:C, ATP, LPS, or Nigericin. Three validated inflammasome inhibitors, A-804598 (P2X7 inhibitor), MCC950 (NLRP3 inhibitor), and disulfiram (gasdermin D inhibitor) were used to demonstrate control of the system. IL-1β levels in collected supernatants indicate that none of the tested stimuli required a priming step, and they induced inflammasome activation to varying levels (Figure 1G). MCC950 effectively inhibited IL-1β release for all stimuli, including flagellin and MDP, suggesting these stimuli may lead to NLRP3 activation either directly[17,18] or following pyroptotic release of DAMPs and other signaling molecules from neighboring cells.[5,6] Disulfiram similarly blocked IL-1β release across all conditions, which is expected given its late, post-pathway convergence mechanism of action (MoA), and also provides evidence that inflammasome signaling was maintained at a controllable level in this assay. Conversely, A-804598 showed strong effects only under ATP activation, which aligns with its specificity for an ATP receptor (P2X7; Figure 1G).

High content images of the activated cells were collected following fixation and staining with a palette that included a subset of traditional cell painting dyes and an antibody used to detect ASC by indirect immunofluorescence. Automated measurement of ASC speck features known to be associated with inflammasome complex activation and formation,[19,20] including speck presence, area, and cellular distribution, were used to assess activation at the single-cell level (Figure 1H). All six activation conditions induced statistically significant increases in ASC speck counts without altering speck area or distance from the center of the cell across 12 independent PBMC donors (Figures 1I, 1J, S1A, and S1B). Corroborating the IL-1β findings, these activators induced a range of ASC speck positivity in treated cells that was sensitive to MCC950 and disulfiram across all conditions (Figures 1I and 1J), and to A-804598 in ATP activated cells (Figure 1J).

Altogether, we validated an imaging-based *in vitro* system in PBMCs that served as the foundation for using ML to define mechanistically distinct inflammasome cellular states that could in turn be used to surface inflammasome compound modulators.
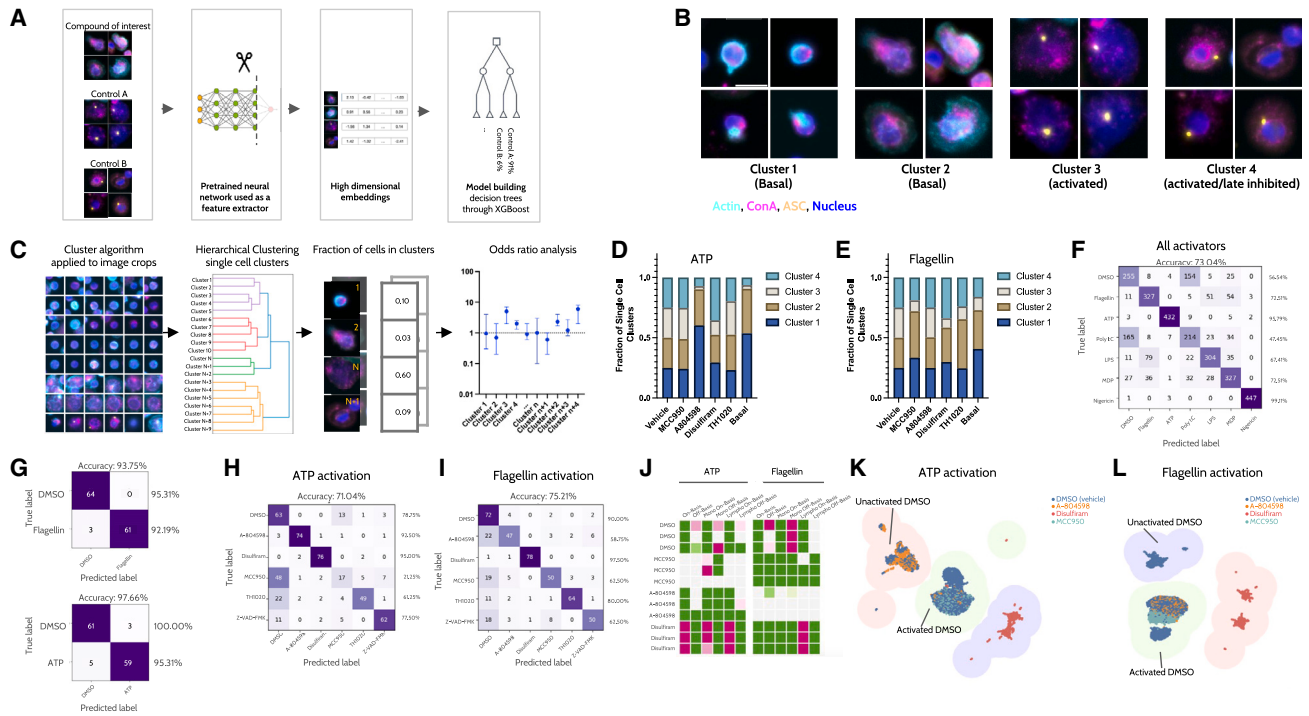
Figure 2. Developing machine learning tooling to measure inflammasome states from imaging data

(A) Schematic of extracting embeddings from images of human PBMCs.

(B) Representative images of cells predicted to belong to clusters 1–4 as indicated. PBMCs stained with Phalloidin, Concanavalin A, anti-ASC, and Hoechst. All images are the same zoom; Scale bar, 10 μm.

(C) Schematic of process for identifying morphological clusters and their associations with inflammasome activation and inhibition. See also Figure S3.

(D) Average median frequency of cells positive for clusters 1–4 following treatment with control inflammasome inhibitors of ATP activated PBMCs. Data shown as average over n = 15 experiments of the within-experiment median of 16 replicates for each of two donors. Each cluster was normalized as a percent of vehicle control and scaled as a fraction of 1 to visualize relative compositional changes between treatment groups.

(E) Same as D, but under flagellin activation.

(F) Confusion matrix of deep learning classification model of inflammasome activation states on human PBMCs using image embeddings. Overall model accuracy shown above the matrix, class specific accuracies displayed to the right. The morphological profile is the well representation obtained by median-averaging VGG16 embeddings of each cell detected in the well.

(G) Binary confusion matrix of deep learning classification model of basal vs. flagellin (top) or ATP (bottom) inflammasome activation states on human PBMCs using image embeddings.

(H) Confusion matrix of deep learning classification model of inflammasome inhibition states on ATP activated human PBMCs using deep learning morphological profiles as input. Overall model accuracy shown above the matrix, class specific accuracies displayed to the right. The morphological profile is the well representation obtained by median-averaging VGG16 embeddings of each cell detected in the well.

(I) Same as H, but under flagellin activation.

(J) Ranking software view of compound mediated on and off basis effects on ATP and flagellin activated PBMCs. Data shown represent the difference (p value) of each condition relative to the activated vehicle control of 16 replicates for each of two donors and across three experiments (each row is an experiment). Analyses shown for individual cell types (monocytes, lymphocytes) as described in the methods, and all cells and shown as relative p values calculated using two-tailed t tests. Data are organized in a matrix with features along the x axis and compound treatments along the y axis. Colors indicate directional change (magenta: decrease, green: increase) and intensities vary by statistical confidence.

(K) UMAP of deep learning morphological profiles from ATP activated cells. Clusters of inhibitor treated cells are colored and indicated in the figure.

(L) UMAP of deep learning morphological profiles from flagellin activated cells. Clusters of inhibitor treated cells are colored and indicated in the figure. See also Figure S3.

Morphologically distinct cell subtypes identified from unsupervised cluster analysis can be used to resolve different stages of inflammasome signaling

To develop ML-based tooling, we first generated high-dimensional statistical representations, called embeddings, from images of PBMCs (Figure 2A). Embeddings are distinct from features derived from classical cell painting pipelines such as CellProfiler[21] in that they are extracted from neural networks that allow ML algorithms to use all the data in an image rather than being limited to predefined features. From embeddings, imaged cells were assigned to cellular subclasses using cell type classifiers that were developed using insights gained from previously performed unsupervised cluster analysis.[22] All subsequent PBMC analyses in the present study were performed on lymphocytic and monocytic subclasses as well as an aggregation of all cells.

We next applied hierarchical clustering to single-cell embeddings to identify phenotypically distinct cell subtypes (PDCS).

Using odds ratios (OR) to assess cluster membership, we found four independent PDCSs that significantly correlated with basal or inflammasome activation conditions (Figures 2B, 2C and Figures S3A and S3C).

The first two of these clusters were associated with the basal state and had OR of 2.66 for cluster 1 and 1.64 for cluster 2. Both clusters 1 and 2 had decreased membership and OR of less than 1 with activated cells, indicating that cells shift away from these clusters upon inflammasome activation (Figures S3C and S3D). Additionally, ASC speck positivity was lower in cluster 1 under activation conditions relative to the global, unactivated population (0.08% cluster 1 vs. 0.4% unactivated [all cells] vs. 2.72% aggregated ATP and flagellin activated [all cells]); Figure S3C), while cluster 2 ASC positivity under activation conditions was comparable to the global, unactivated population at 0.4%.

In contrast, clusters 3 and 4 were statistically associated with activation. Specifically, cluster 3 had a low OR with the basal state (0.13) and low membership frequency, but was conversely associated with increased membership frequency, ASC positivity, and higher OR under activation conditions (OR: ATP 2.13, flagellin 1.60; ASC aggregated ATP and flagellin: 40.1% cluster vs. 2.72% all cells). Cluster 3 cells appear large with faint mitochondrial and nuclear signals and resemble pyroptotic monocytes.[23] Cluster 4 cells appear to be enlarged and monocytic (Figure 2B), and were negatively associated with the basal state (Figure S3D; OR: 0.38). Cluster 4 membership frequency and ASC positivity were also enriched relative to both activation conditions (ASC aggregated ATP and flagellin: 7.7% cluster vs. 2.72% all cells), and had a high OR (2.6) with ATP activation (Figures 2B, S3C and S3D).

We next determined whether quantification of PDSCs could serve as a readout for compound potency and mechanism by measuring control inhibitor mediated shifts in cluster membership. The P2X7 inhibitor control A-804598 induced significant increases in membership to basal-associated clusters 1 (353% vehicle +/− 40.44% standard error of the mean [SEM]) and 2 (175% vehicle +/− 9.9% SEM), and reduced membership to activation-associated cluster 3 (15.78% of vehicle +/− 2.5% SEM) relative to ATP activated control (Figure S3F). These findings were validated by a decrease in ASC positivity in cluster 3 following A-804598 treatment relative to ATP activated vehicle (9.2% vs. 11.5% vehicle). In contrast, A-804598 treated cells shared nearly identical cluster membership and ASC positivity in all clusters relative to flagellin activated control (Figures 2D, 2E and Figures S3E–S3G), which is expected given the ATP specificity of P2X7.

TH1020, MCC950, and disulfiram all similarly shifted flagellin, but not ATP, activated cells toward basal-associated clusters 1 and 2 with little effect on activation-associated cluster 3 in ATP treated cells, despite reducing its ASC positivity (11.55% vehicle vs. 1.8% disulfiram vs. 1.2% MCC950 vs. 0.92% TH1020). Under flagellin activation, however, they lowered cluster 3 membership (MCC950: 32.37% +/− 4.43 SEM; disulfiram: 33.48% +/− 4.55 SEM; TH1020: 35.02% +/− 5.19 SEM all compared to 100% vehicle) and ASC positivity (70.9% vehicle vs. 14.8% disulfiram vs. 52.8% MCC950 vs. 29.9% TH1020).

These data indicate that inhibitors that act downstream of signal initiation suspend cells in activated states, an effect that would be more evident following stimulation with activators like ATP that mediate modest responses and whose morphological profiles are dominated by the primary activation signal (Figures 2D, 2E and Figures S3E–S3G). In contrast, the morphological profile of a more potent activator like flagellin (Figure 1G) may be dominated by neighboring cells that secondarily respond to pyroptotic release of proinflammatory signals, and would therefore be more sensitive to inhibitor-induced compositional shifts when the secondary response is blocked. PDSC membership frequency can therefore be used to resolve these effects and identify compound mechanisms of action at various stages of activation.

Similar to cluster 3, frequency of cells belonging to cluster 4 decreased following MCC950 and TH1020 treatments on flagellin activated cells, and A-804598 treatment on ATP activated cells. Disulfiram, however, shifted activated cells into cluster 4 (ATP: 144.57% +/− 21.98 SEM; flagellin: 144.02% +/− 17.67 SEM; compared to 100% vehicle) while lowering its ASC positivity (ATP: 5.5% vehicle vs. 1.7% disulfiram; flagellin: 28.6% vehicle vs. 0.89% disulfiram). Therefore, disulfiram inhibits inflammasome signaling, but shifts cells into cluster 4. This indicates that cluster 4 membership can be used to resolve very late pathway inhibitors from those whose targets lie upstream of gasdermin D (Figures 2D, 2E; Figures S3E–S3G).

Altogether, PDSC membership can be used as cell biological readout for identification and quantification of various stages of inflammasome signaling.

Trained classification models resolve a spectrum of inflammasome activated and inhibited cellular states in human PBMCs

We built a classification model to predict the perturbation applied to the cells in a given well. The morphological profiles for each well are used as input to an XGBoost classifier, while the target mutually exclusive classes are the six inflammasome stimuli described previously: MDP, flagellin, Poly I:C, ATP, LPS, and nigericin. The training and validation strategies, as well as the morphological profile definition, are detailed in the Methods section. Each activator was tested on 24 independent donor samples to account for biological diversity and ensure models learn from inflammasome relevant features that are independent of donor differences. All model results are reported using a 4-fold cross validation approach, where each fold is defined by training the model on 18 donors, and tested on 6 donors unseen in the training set. The resulting model performed with an average accuracy of 73.04% +/− 1.2 SD and can therefore reliably differentiate between activation states. Notably, flagellin, ATP, and nigericin predictions were all above 90% accuracy (Figure 2F). Importantly, we also trained a model to determine whether inflammasome activation states are distinct from other cellular stresses in PBMCs. To do this, we compared the response of PBMCs to flagellin with other death-inducing compounds, including staurosporine, digoxin, elesclomol, lanatoside C, darapladib, and doxorubicin, which have been shown to induce apoptosis, necrosis, and other types of cell death. Our model successfully discriminated between these compounds with 78.2% accuracy, with some expected confusion between

lanatoside C and digoxin, which are both glycosides extracted from digitalis plants (Figure S1C).

We next selected ATP and flagellin as stimuli for the downstream screening effort due to their specific and robust responses and trained binary classifiers on PBMCs to distinguish between basal and ATP or basal and flagellin activated PBMCs (Figure 2G). These classifiers perform with very high accuracy (flagellin overall accuracy of 93.75%, and ATP overall accuracy of 97.66%) and confidently predict the basal and activated states. Further, focusing on ATP and flagellin allowed us to interrogate two different biological pathways that cover DAMP and PAMP stimuli.

We also trained models to discriminate between inflammasome inhibition states on ATP- or flagellin-activated PBMCs using the following established inhibitors: MCC950, disulfiram, A-804598, TH1020, Z-VAD-FMK (caspase 1 inhibitor), and DMSO (vehicle control). Overall model accuracy was 71.04% for ATP and 75.21% for flagellin-activated conditions (Figures 2H and 2I). A-804598 expectedly showed significant confusion with flagellin-activated vehicle but had high accuracy (92.50%) on ATP-activated cells. Interestingly, MCC950 showed confusion with the ATP-activated vehicle (48/80 wells), and to a lesser extent with flagellin-activated vehicle (19/80 wells). This again validates the hypothesis that MCC950 suspends inhibited cells in an activated state, and this effect is more pronounced when there is limited secondary activation from pyroptotically released molecules, such as what is observed with ATP stimulation. Disulfiram classification had relatively much higher accuracy, likely because it acts much farther downstream and induces unique, distinguishable states of cellular inhibition, such as what was seen with cluster 4 enrichment.

Projection scores assess similarity and dissimilarity to control activated or basal states in PBMCs

In addition to training classifiers, we evaluated compounds using on- and off-basis scores. These scores were generated with the same normalized well profiles used for the classifiers, and analyzed using a geometric approach whereby a basis vector is first established in the embedding space that leads from activated data to basal, non-activated data (one vector per activation condition; vehicle and plate-level controlled).

Subsequently, the on-basis scores for a given compound under an activation condition is calculated by first generating a vector from the vehicle-activated control to the compound in question, then taking the normalized scalar projection of that vector onto the basis vector for the given activated vehicle-control. The resulting output is a singular, scalar value, where 1.0 is interpreted as identical to the basal state, 0.0 is interpreted as identical to the activated condition, and values in between are fractional blends of the two. Correspondingly, off-basis scores are similarly calculated, but with a normalized scalar rejection. The resulting output is also a singular, scalar value, where larger values represent phenotypic differences orthogonal to the differences between the basal and activated states, and a value of 0 represents no orthogonal phenotypic differences.

Combined model outputs resolve a spectrum of activation and inhibition cellular states in PBMCs from high-content imaging data

Classifier output scores (how a model classifies compound effects) and projection values were used to quantify compound-mediated effects using the activated state as a reference. Here, unactivated and inhibited cells have low activation model scores, and compounds that do not inhibit appear neutral. Compounds that induce effects that are similar to a modeled control inhibitor (such as disulfiram) will have high disulfiram scores, while those that drive differential effects will have low disulfiram scores.

A-804598 had low activation classifier output scores and high on-basis scores relative to vehicle-treated ATP-activated cells, but appeared neutral under flagellin activation, as expected. MCC950 treatment of ATP-activated PBMCs mediated high off-basis and low on-basis scores for monocytes with neutral activation classifier output scores. This combined effect may be due to MCC950 suspending inflammasome sensitive cells such as monocytes in an activated state that cannot progress and that have low ASC positivity. In flagellin-activated PBMCs, however, MCC950 had high on-basis scores and low activation classifier output scores across all cell types, suggesting it retains a proportion of cells in their basal state. Lastly, disulfiram induced high off-basis scores for all ATP- and flagellin-activated cells, low on-basis scores for all ATP-activated cells, and low on-basis scores for flagellin-activated lymphocytes (Figures 2J and S3B), suggesting that inhibition at the final step before pyroptosis orthogonally changes cell morphology.

Execution of a high-content imaging screen of inflammasome activated PBMCs *in vitro* yields functional classes of treated cells

We next scaled these analytical tools and experimental methods into a high content imaging (HCI) screen of ATP- or flagellin-activated PBMCs treated with a 12,000 compound bioactive library with a goal of identifying unique targets and categorizing functionally diverse compound inhibitors (Figure 3A). Plate layouts were designed to maximize compound comparisons and minimize plate and donor variability (Figure S2A). Possible experimental confounders were interrogated by conducting a quality analysis to identify variability across plates, donors, and well locations. Cell counts, stain intensities, and focal quality were calculated for each well. Cell counts and sub-type representation were evaluated in donor control wells to monitor for donor-driven effects (Figures S2B–S2H).

To verify that the morphological profiles captured relevant phenotypic differences, we generated UMAP[24] (Uniform Manifold Approximation and Projections) visualizations. Here, activated and basal states segregated into independent clusters without any obvious clustering driven by donors or experimental confounders (Figures 2K and 2L). Further validation of this was seen in the A-804598 treated wells, which were associated with the basal state while under ATP activation and the activated state while under flagellin activation. Similar to what was observed in the PDCS clusters and classification model outputs, MCC950 treatment closely resembled the activated vehicle control under ATP activation, but it shifted flagellin-activated wells
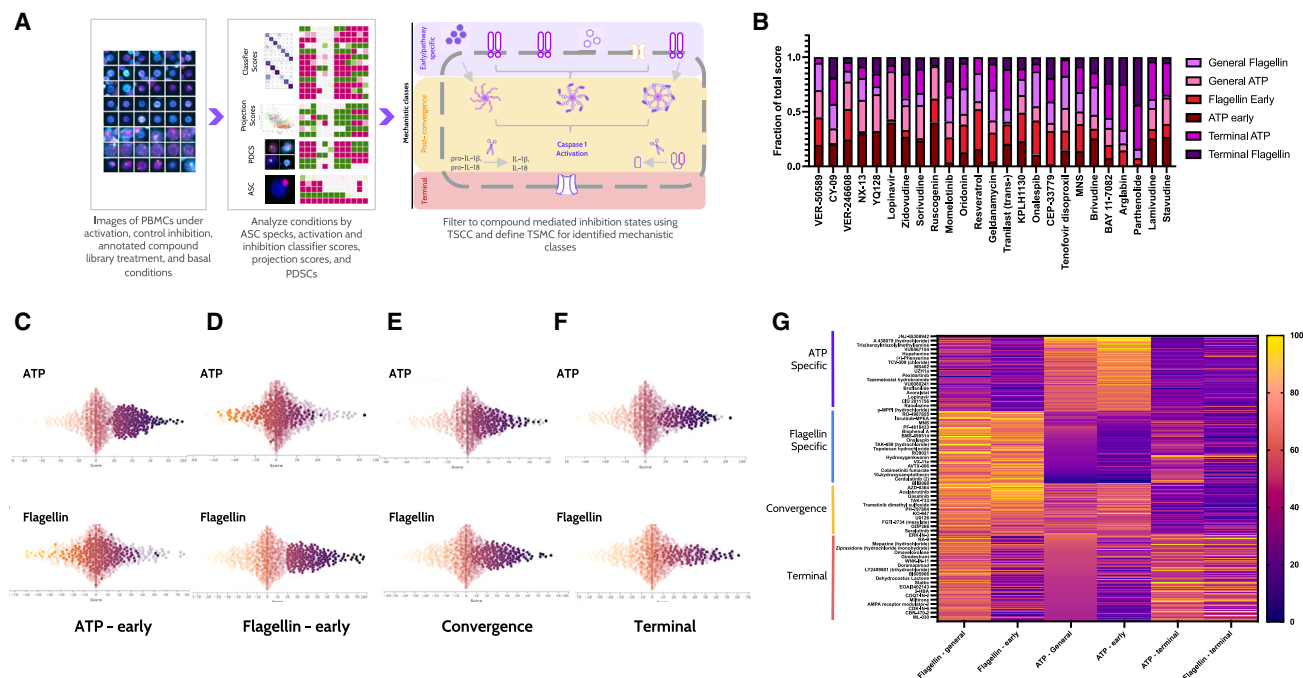
Figure 3. Compound hit identification and mechanistic classification from a high-content imaging screen

(A) Schematic of targeted scoring approach. PDSC = phenotypically distinct cellular subtype; TSMC = targeted scoring minimum criteria; TSCC = targeted scoring categorization criteria.

(B) Breakdown of scores for a set of literature validated inflammasome inhibitors; Z score normalized and plotted as fraction of total for each compound. Does not rank by potency, just predominant mechanism.

(C) General score distribution under ATP or flagellin activation for hits from early ATP class. Hits shown are those that met a stringent TSCC (>20 general score; Early: >120 (sum of general + early per condition) for one condition and relative ATP::Flagellin relationship [(Max-Min/Max)] of at least 0.7; Terminal: general >10, terminal >15 for both ATP and flagellin; Convergent: early scores >70 for ATP and >100 for flagellin, with a relative ATP::Flagellin relationship [(Max-Min/Max)] of <0.7. Color gradient denotes relative scores. The higher intensity points are the selected compounds, while the lower intensity points represent the rest of the compounds tested.

(D) Same as C, but for early flagellin class.

(E) Same as C, but convergence class.

(F) Same as C, but terminal class.

(G) Heatmap showing breakdown of hits meeting the same stringent TSCC as used in C. Rows are compounds grouped by mechanistic class (indicated in brackets), and columns are aggregated scores of each compound. See also Figures S4 and S5.

away from the activated vehicle cluster. Disulfiram-treated wells formed their own distinct groupings under both conditions that were not associated with possible experimental confounders (Figures 2K and 2L).

Holistic scores that integrate ML and cell biological readouts can surface and mechanistically categorize inflammasome inhibitors from high content imaging screen

Compound-mediated effects were analyzed using the methods described previously, namely ASC speck quantification, PDSC membership, and classification model outputs and projection scores. The resulting p values for each readout were ingested into our Ranking software tool where data are organized in a matrix of features and compounds, and where colors indicate directional change and intensities vary by statistical confidence (list of readouts shown in Table S1). Notably, no single readout sufficiently defined the spectrum of inflammasome associated cellular states, so we adopted a comprehensive, hypothesis-

driven targeted scoring (TS) system to aggregate the interpretable biological readouts collected using our various analytical tools and filter hits according to assigned thresholds.

We first designed a general score to establish a targeted scoring minimum criteria (TSMC) for identifying inflammasome inhibitors. This score applied directional weights to the calculated p values for a set of selected ML and cell biological features that are broadly associated with inflammasome inhibition, including a decrease in ASC specks and an increase in alive cells (Figure S4A). A weighted sum of the resulting values was calculated for each compound treatment, and a minimum score of 20 from at least one condition (ATP or flagellin) was set as a minimum threshold that yielded 1,965 potential inflammasome inhibitors (Table S2).

All compounds that met the TSMC were then subjected to a series of scores designed to categorize compounds into the following functional classes: (1) early ATP, (2) early flagellin, (3) shared pathway convergence, and (4) terminal. We also implemented a toxicity score to identify conditions that induce

inflammasome-independent unhealthy or dying cells (Figure S4A). 1,018 of the 1,965 compounds that met the minimum threshold using the general score criteria also met the TS classification criteria (TSCC) required to be assigned a mechanistic class, and 112 of those were flagged as potentially toxic (Table S2). This yielded an overall hit rate of 7.55%, which is not unexpected from a phenotypic bioactive library screen where all compounds have been demonstrated to have biological effects, and where the screening criteria are not limited to a specific target(s).[25] Importantly, a set of literature-validated inhibitors, including CY-09,[26] tenofovir,[27] and ruscogenin,[28] as well as compounds targeting P2X7, NRTI,[27,29] HSP90,[30] PDHK,[31] or BTK[32] had positive general scores (Figures 3B and S4B), substantiating our experimental and analytical methods.

General score distributions for top scoring compounds assigned to the ATP or flagellin early classes showed high relative condition-specific scores compared to all compounds, and low relative terminal and toxicity scores. These same compounds adopted neutral distributions for all scores relative to the general population in their respective non-effective conditions. Convergence was determined by positive general score distributions under both activation conditions, and neutral to negative terminal and toxicity scores. The terminal inhibitor class had similar general score distributions under both conditions, but had relatively high terminal scores (Figures 3C–3F and Figures S5A and S5B).

Mechanistic classes are clearly delineated in a heatmap of top scoring compounds, where compounds are ordered by their functional classes on the y axis and their normalized scores on the x axis (Figure 3G). Altogether, these data demonstrate that this approach can be used to mechanistically define induced cellular changes from an HCI phenotypic screen to surface and categorize hits.

A hypothesis-free method using morphological profile shifts can be used to identify and validate screening hits

As a parallel approach, we utilized a hypothesis-free analysis in the feature space defined by compound morphological profiles. Morphological profiles were Z scored against the activated vehicle control distribution for the corresponding donor, plate and activator, so activated control profiles are normally distributed, and the Euclidean norm of the profile vector represents the overall distance from the average activated control profile.

Compound mediated distribution shifts (CMDS) of morphological profile vector norms in different activation conditions can be used for mechanistic compound classification. For example, disulfiram mediated distributions were significantly different from both ATP- and flagellin-activated states, while A-804598 exhibited a significant distribution shift only under ATP activation. TH1020 distribution deviated strongly from flagellin-activated control, but it also induced a radial shift away from ATP-activated control. In alignment with the classification models and morphological cluster profiles, MCC950 mediated distribution changes in flagellin-, but not ATP-, activated wells (Figures 4A–4D; Figures S6A–S6D).

Four quadrants were defined in the morphological profile norm plane using the 99th percentiles of activated DMSO as thresholds. Here, compounds that mediated shifts above the threshold for both activation states were called late stage inhibitors, while those with single condition effects were called early or pathway specific inhibitors, as exemplified by the control compounds (Figures 4E and 4F).

We next used CMDS to cross-validate hits from the hypothesis driven TS approach. Importantly, this measurement surfaces any induced differences that are greater than biological variability of activated DMSO, so to focus on inflammasome relevant functions, we applied the toxicity score and ASC speck measurement as filters to generate a list of 2,037 potential inflammasome inhibitors (Table S3). The literature-validated compounds highlighted previously using the TS method performed similarly using CMDS, demonstrating that this method reliably surfaces inflammasome inhibitors (Figures 4G and S6E).

1,142 of the CMDS identified compounds also met the TSMC of 20, which shared a 78.9% overlap with the hits generated using the TS method and meeting the same toxicity and ASC speck thresholds. 534/895 (64.35%) of the CMDS compounds that did not meet the TSMC of 20 had general scores above 10 and would have been TSMC hits if the scoring criteria had been lowered by half. Similarly, a majority of the non-overlapping TS identified compounds (219/367; 60%) that did not meet the 99th percentile CMDS criteria met a looser 95th percentile cutoff (Figure 4H). Thus, there is strong agreement between the hypothesis-independent CMDS method and hypothesis-dependent TS method. This alignment was remarkably strong with the compounds that induced changes meeting the TSCC, where there was 91.1% overlap with CMDS (Figure S4A and Table S3).

As described previously, the CMDS method can be used to define early and late inflammasome inhibition states. 98.7% of non-toxic TSCC compounds classified as convergent or terminal inhibitors were also categorized as late pathway inhibitors using the CMDS method. There was less agreement for condition-specific compounds, which is likely due to the fundamental differences in how thresholds were set. In order to identify activation-specific inhibitors, the CMDS method requires significant compound mediated differences in either ATP or flagellin activated cells and explicitly not the other. The TSCC method, however, defines compounds as pathway specific if they predominantly induce effects under one activation condition, but allows them to mediate some phenotypic changes in the other. Thus, most of the compounds classified by TSCC as condition-specific were classified as late pathway inhibitors by CMDS. Altogether, the CMDS approach can be used to identify functionally distinct inflammasome inhibition states and validate hypothesis driven discovery methods.

Raf-MEK-ERK and HSP90 are potential mediators of inflammasome signaling as revealed by compound annotation enrichment and cosine similarity

Within the bioactive compound library, there are many instances where multiple compounds are annotated as modulators of the same target. We used these annotations to surface targets that are important for inflammasome signaling. To be considered, targets had to have at least 5 annotated compounds in the library and at least 2 compounds identified as hits. Target enrichment was calculated as the percentage of compounds in the hit list divided by the percentage of compounds in the library.
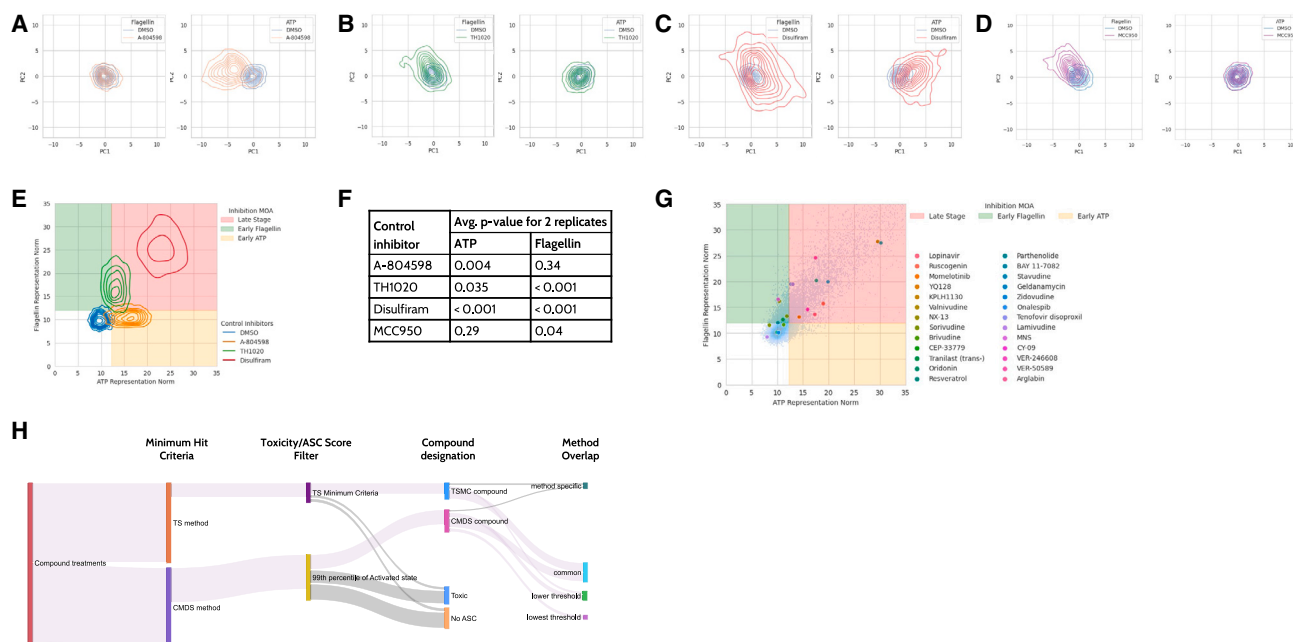
Figure 4. Compound mediated distribution shifts (CMDS) of morphological profiles to identify and characterize inflammasome inhibitors

(A–D) Comparison of control inhibitors and DMSO distributions for ATP and flagellin activation in the plane defined by the first two principal components of the morphological profile.

(E) Comparison of control inhibitors and DMSO distributions in the plane defined by the norm of the morphological profile vector under ATP activation (x axis) and flagellin activation (y axis).

(F) For each control inhibitor the fraction of replicates beyond the 95th percentile of the DMSO distribution is reported alongside the average p value obtained by comparing two randomly sampled replicates against the DMSO distribution (null hypothesis) using Welch's t test.

(G) CMDS of morphological profiles of literature validated inflammasome inhibitors.

(H) Sankey chart showing hit designation for the distance based and targeted scoring methods, and alignment of methods (purple flow). See also Figure S6.

Unsurprisingly, compounds targeting P2X7 had a very high enrichment factor of 13.4x under ATP activation. Interestingly, 3 of the 10 targets with greater than 4x hit-enrichment under flagellin activation belong to the Raf signaling pathway, strongly implicating this pathway in inflammasome signaling. HSP90, which has been shown to stabilize Raf, had an enrichment factor of 8.1 (Figures 5A and 5B).[33,34] Raf and HSP90 were also on the ATP activation list, implicating these targets in multi-pathway MoAs.

We next assessed whether compounds annotated to hit the same target are phenotypically similar to validate their MoAs and targets. To do this, we first measured cosine similarity[35] between Z score normalized morphological profiles under the flagellin activation condition. For example, HSP90 inhibitors were found to be strongly enriched in the hit list, and five out of seven compounds surfaced from the screen were predicted to have close similarity to each other, while two diverged (Figure 5E). We then compared TSCC scores and found that the five compounds with the most similarity had high general, low terminal, and low toxicity scores for both conditions. The two divergent compounds, however, had high toxicity and terminal scores (Figure 5F), supporting use of these metrics to confirm target mechanisms and identify phenotypically similar compounds.

Similar analyses were performed on Raf, MEK, and ERK compounds to calculate similarity at both the target and pathway levels. As shown in Fig 5G and A set of MEK inhibitors have

strong similarity to each other as well as to subsets of Raf and ERK inhibitors, demonstrating that these compounds perform similarly and validating this pathway as integral to inflammasome signaling. TSCC scores indicate that these compounds mechanistically act on both ATP and flagellin activated cells, with some preference for flagellin and generally with low toxicity (Figure 5H). These screening data suggest that HSP90 inhibitors as well as compounds targeting the Raf-MEK-ERK signaling pathway are involved in a step shared by multiple pathways or are involved in secondary activation of NLRP3 following pyroptotic release of DAMPs and other signaling molecules.

Compound testing across several activation conditions in PBMCs validates and refines mechanistic classifications of screening hits

To hone mechanistic classification of top hits and implicate specific targets in inflammasome signaling, we generated a list of 299 compounds to test across several activation conditions in PBMCs. 234 compounds were selected based on high screening scores for each of the functional classes, 50 compounds were selected based on enriched target annotations, and 15 compounds were selected based on high cosine similarity scores to enriched targets (Table S4).

Each compound was tested on PBMCs independently activated with the six stimuli described above (ATP, flagellin,
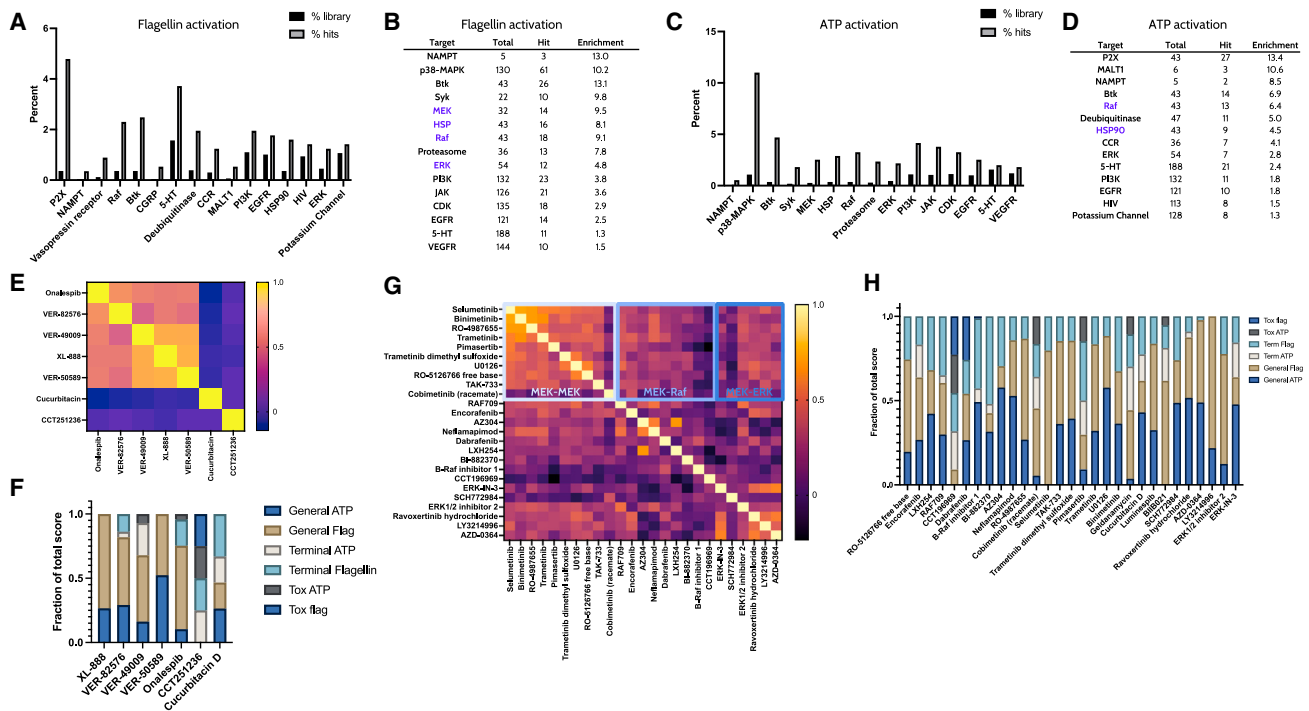
Figure 5. Target and pathway discovery using enrichment scores and cosine distances from screening data

(A) Targets with more than 5 compounds in the library and which were present on the flagellin activated list. Shown as percent total compounds in the library (black) relative to percent compounds on the hit list (gray).

(B) Table detailing the number of compounds represented by target in the library and in the hit list under flagellin activation. Also shown is the calculated enrichment value (% hit/% total).

(C) Same as A, but for ATP.

(D) Same as B, but for ATP E. Heatmap of similarity scores from 25 μM HSP compounds on flagellin activated PBMCs using Z score normalized cosine distances.

(F) Targeted scoring visualized as fraction of total score for HSP inhibitors validates similarity score findings.

(G) Heatmap of similarity scores from 25 μM Raf, MEK, and ERK compounds on flagellin activated PBMCs using Z score normalized cosine distances.

(H) Targeted scoring visualized as fraction of total score for Raf, MEK, and ERK inhibitors validates similarity score findings.

LPS, nigericin, Poly I:C, MDP), and cells were fixed, stained, and imaged. Image embeddings were extracted and analyzed as before, and resulting data were ingested into our Ranking software tool to assess and score compound-mediated effects.

Directional weights of features associated with various convergence points across the six inflammasome pathways were used to generate the following scores for compound classification: (1) general, (2) early pathway, (3) MCC950 similarity, (4) late/GSDMD, (5) convergence, (6) high on-basis, and (7) high off-basis. A pathway multiplier (the sum of conditions with positive general scores) was also calculated for each compound (score details in Figures S7B and S7C).

A Pearson's correlation matrix of compound scores was generated for each of the six conditions and clustered using Ward's method (Figure 6A). These hierarchical data informed how individual scores were aggregated for determining five functional classes of inhibitors, ATP early, flagellin early, early convergence, convergence, and terminal. Inhibitors were graded using each score and assigned to their respective maximally scored class.

On-basis and early pathway scores clustered together with positive correlation (Figure 6A), and were therefore used to identify three classes of compounds: those that are specific for (1)

ATP or (2) flagellin, and (3) those that act at an early pathway convergence point and retain cells in their basal states across multiple activation conditions. It is important to note that since all tested compounds were first screened for ATP or flagellin inhibition, we did not surface pathway-specific inhibitors for the other activators. Rather, these stimuli were used to characterize compounds that suspend cells following pathway convergence points or that inhibit secondary signaling by pyroptotically released molecules. Of the 299 compounds that were tested, 72 suspended cells early in either the ATP or flagellin activation states (31 ATP, 41 flagellin), and 61 inhibited cells following early pathway convergence points (Table S4). These classes are distinguishable by principal-component analysis (PCA) and easily visualized in a heatmap where compounds are ordered on the y axis according to their assigned mechanistic classes and on the x axis by their respective aggregate or condition-specific scores (Figures 6B, 6C and Figure S7A).

A fourth class of late pathway, convergent compounds was based on positive associations between on-basis and MCC950 scores and concurrent negative correlations with terminal scores (Figure 6A). The on-basis, MCC950, and negative terminal scores were combined using a directionally weighted sum for each condition. Positive Z scored values per condition
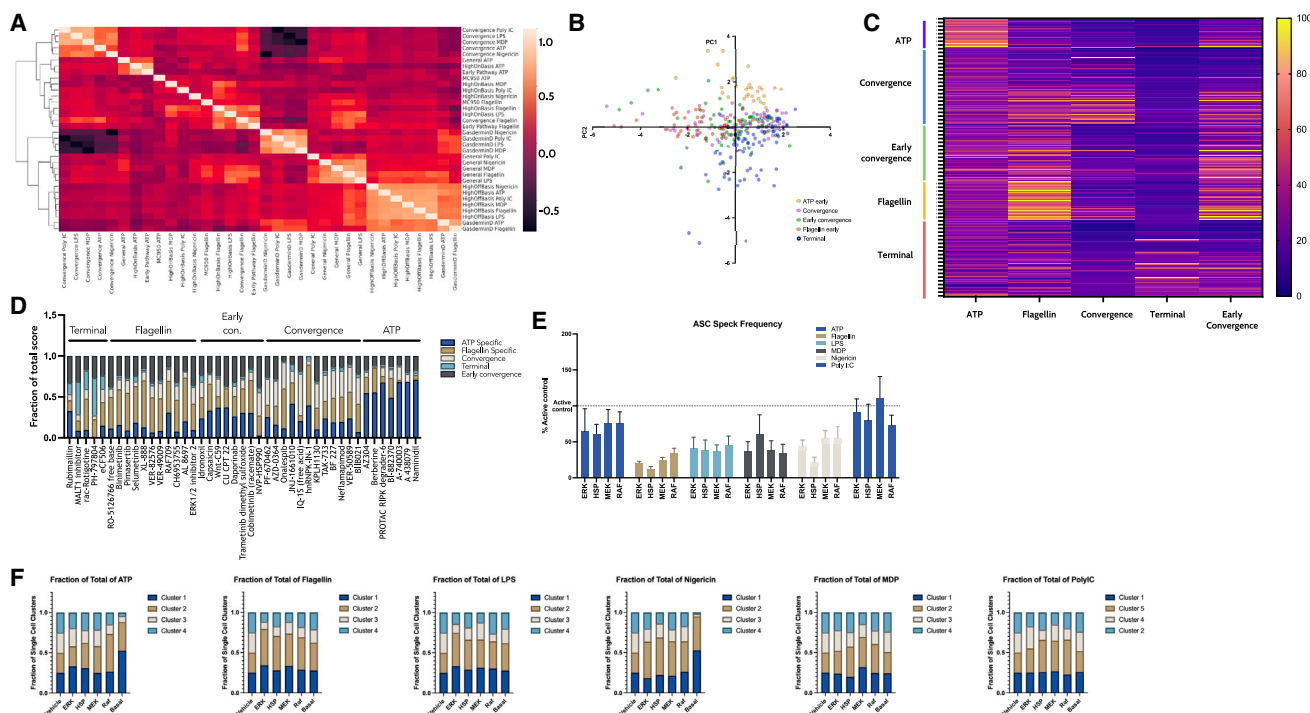
Figure 6. Mechanistic classification of inflammasome inhibitors from multi-activator imaging data

(A) Correlation (Pearson's) heatmap of hierarchically clustered individual targeted scores (Ward's method) applied to human PBMCs independently activated with 6 inflammasome activators from 9 independent experiments.

(B) PCA of aggregated scores applied to data from 299 compounds on human PBMCs independently activated with 6 inflammasome activators from 9 independent experiments.

(C) Heatmap of compound aggregated scores. Rows are ordered categorically by assigned mechanistic classes, and aggregate scores are arranged on the y axis.

(D) Breakdown of scores for a subset of top inflammasome inhibitors; Z score normalized and plotted as fraction of total for each compound. Does not rank by potency, just predominant mechanism.

(E) ASC quantification of Raf, MEK, ERK, and HSP90 target classes. Median frequency of ASC specks was quantified for individual compound treatments (at 20 μM) and then aggregated as target classes consisting of 3–5 individual compound treatments. Data shown as average median of 7 replicates across each of 2 donors with standard error and normalized as a percentage of the active control for each condition.

(F) PDSC compositional shifts for Raf, MEK, Erk, and HSP90 target classes for ATP, MDP, Nigericin, PolyIC, LPS, and flagellin. Median cluster membership was calculated from 7 replicates for each of two donors for each compound and then aggregated as an average target class. Each cluster was normalized as a percent of vehicle control and scaled as a fraction of 1 to visualize relative compositional changes between treatment groups. See also Figures S7, S8, and Table S4.

were then averaged with the pathway multiplier into a single output (Figure S7C). 82 compounds were assigned to this class, and defined as those that inhibit multiple stimuli and suspend cells in activated states.

The fifth class captured terminal inhibitors and was calculated using a weighted sum for each condition based on the finding that late/GSDMD scores had strong positive correlations with off-basis scores, and negative correlations with convergence scores (Figure 6A). An aggregate score was calculated from the average of the pathway multiplier plus the positive Z scored values from each condition. 84 compounds were found to suspend cells in terminally inhibited states that look dissimilar to basal and activated states (Figure 6C and Table S4).

Altogether, these analyses demonstrate that mechanistic differences between inflammasome inhibitors can be resolved from imaging data. This is further supported when looking at stacked bar charts showing the breakdown of the five scores for representative compounds from each class (Figure 6D).

Here, the ATP or flagellin specific inhibitors show clear enrichment in those respective classes, with very convergence or terminal scores. Terminal scores, conversely, are enriched in compounds with very low pathway specific or convergence scores, demonstrating clear distinctions in MoA between these classes.

The Raf pathway is implicated in inflammasome signaling by consistent mechanistic classification of compounds targeting Raf-MEK-ERK and HSP90

We next used these scores to mechanistically characterize enriched targets and assess pathway contributions to inflammasome signaling. P2X7 inhibitors exemplify this approach as these were expectedly enriched only in the ATP-specific class (Figure S8A and Table S4).

A total of 34 compounds targeting different proteins in the Raf-MEK-ERK pathway were tested in this assay. Interestingly, they predominantly fell into two functional classes: early flagellin

inhibitors or early convergent inhibitors (Figures 6D and S8A). HSP90 inhibitors were similarly classified, in addition to a subset being designated as downstream convergent inhibitors (Figure 6D; Table S4 and Figure S8A). These classifications are largely based on the ability of these compounds to restore cells to a basal state as shown by their induced increase in on-basis scores, especially under flagellin activation, and frequently also under robust activation with LPS or nigericin (Figure S8B).

Aggregating individual compound data into target specific groups for ERK, MEK, Raf, and HSP90 generally indicates that the Raf pathway is involved downstream of the convergence of multiple activators as shown by strong ASC speck inhibition relative to the activation control, especially under more robust activation conditions such as flagellin, LPS, and nigericin. This provides support that these compounds generally act downstream of a convergence point across multiple inflammasome activators and can inhibit amplification of a strong inflammasome stimuli (Figure 6E).

We also assessed compositional shifts of the inflammasome associated cell subtypes by these aggregated compound groups across all conditions. Similar to what was observed for ASC specks, inhibition of Raf pathway members induces clear shifts toward the basal state clusters for all conditions, especially cluster 2, with corresponding reductions in cluster 4, supporting a MoA that lies upstream of GSDMD pore formation and the terminal steps of pyroptosis, but downstream of activator convergence points (Figure 6F). This is further supported by the on and off basis signatures for these compounds, which are aligned with MCC950 and the basal DMSO control for multiple conditions (Figure S8B).

Mechanistically distinct hits are validated as potent inflammasome inhibitors in an orthogonal primary human monocyte assay

We next selected 120 compounds that represented the top hits and enriched targets from each of the classes defined aforementioned (Table S5) for orthogonal validation on ATP- or flagellin-activated primary human monocytes. Notably, these hits were designated as the most likely to be true and specific inflammasome inhibitors and represent approximately 1% of the original screening library.

Primary human monocytes were activated with flagellin or ATP, treated with the selected compounds, and stained with the viability stains Annexin V and SYTOX green to distinguish between pyroptosis and apoptosis. Images of cells were analyzed using supervised classification into the following three categories: (1) healthy/alive, (2) apoptotic, and (3) pyroptotic (Figure 7A). IL-1β levels in the supernatants were also measured to confirm inflammasome activation.

Validating these readouts, we observed that ATP and flagellin stimulation each drove significant increases in pyroptotic cells and corresponding decreases in healthy cells relative to the basal condition (Figures 7B, S9A and S9B). They also significantly reduced the number of apoptotic cells, indicating the decrease in healthy cells was not due to increased apoptosis. MCC950 inhibited pyroptosis in both ATP- and flagellin-activated cells, while A-804598 demonstrated ATP specificity (Figure 7C).

101/120 (84.2%) of the test compounds effectively inhibited inflammasome activation under at least one condition, as determined by a simultaneous increase in the percentage of alive cells, a >50% decrease in pyroptosis, and a >30% reduction of IL-1β relative to the respective activated states (Figures 7E and 7F; Figures S9G and S9H and Tables S5 and S6). These thresholds were sufficient to resolve true inhibitors, as shown by distinct PCA clusters (Figure 7D). 17/19 of the non-inhibitory compounds lowered IL-1β levels by more than 30% in at least one condition, but they did not meet the pyroptosis or viability criteria (Figures 7E, 7F and Figures S9G and S9H). Importantly, these data substantiate the efficiency and accuracy with which our experimental and analytical methods surfaced potent inflammasome inhibitors.

We then assessed the potency of a set of top compounds representing each mechanistic class: (1) A-740003 (ATP), (2) Selumetinib (flagellin), (3) NVP-HSP990 (early convergence), (4) KPLH1130 and onalespib (convergence), (5) rubimaillin (terminal). A-740003 demonstrated strong ATP condition specificity by increasing the number of alive cells, lowering the number of pyroptotic cells, and blocking IL-1β release in a dose dependent manner only under ATP activation. Similarly, selumetinib inhibited pyroptosis and increased viability under only flagellin activation conditions (Figures 7G–7I; Figures S9C–S9F and Table S6).

NVP-HSP990 inhibited pyroptosis and IL-1β release under both activation conditions without inducing apoptotic cell death in monocytes. Onalespib and KPLH1130 represented the late convergent compound class and each mediated strong, dose-dependent inhibition of IL-1β and pyroptosis while increasing the number of alive cells under both ATP and flagellin activation (Figures 7G–7I; Figures–S9F). Rubimaillin (ACAT1 inhibitor), the representative terminal inhibitor, increased viability without increasing apoptotic cell counts under both conditions (Figures S9C–S9F). It should be noted that in this monocytic assay, the terminal compounds performed similarly to the convergent classes of inhibitors, which further validates our upstream process to discriminate between mechanistically distinct inhibitors.

Raf-MEK-ERK and HSP90 can be targeted to potently inhibit inflammasome activation

We next selected 3 compounds targeting each of Raf, MEK, ERK, or HSP90 to determine the general potency of Raf pathway involvement in inflammasome signaling in primary monocytes. Notably, these compounds all passed the thresholds set aforementioned for inhibiting pyroptosis without shifting cells toward apoptosis.

All of the selected inhibitors along the Raf-MEK-ERK axis showed strong, dose-dependent inhibition of IL-1β release and pyroptosis under flagellin activation (Figures 8A and 8B), and to a lesser extent under ATP activation (Figures 8C and 8D). HSP90 inhibitors similarly showed higher potency on flagellin activated cells for IL-1β release (Figures 8E–8H), demonstrated by flagellin inhibition curves shifted to the left of ATP activated curves. Altogether, these data demonstrate that inhibiting the Raf signaling pathway is a potent and direct means of blocking inflammasome signaling without introducing toxicity or shifting cells to another form of cell death.
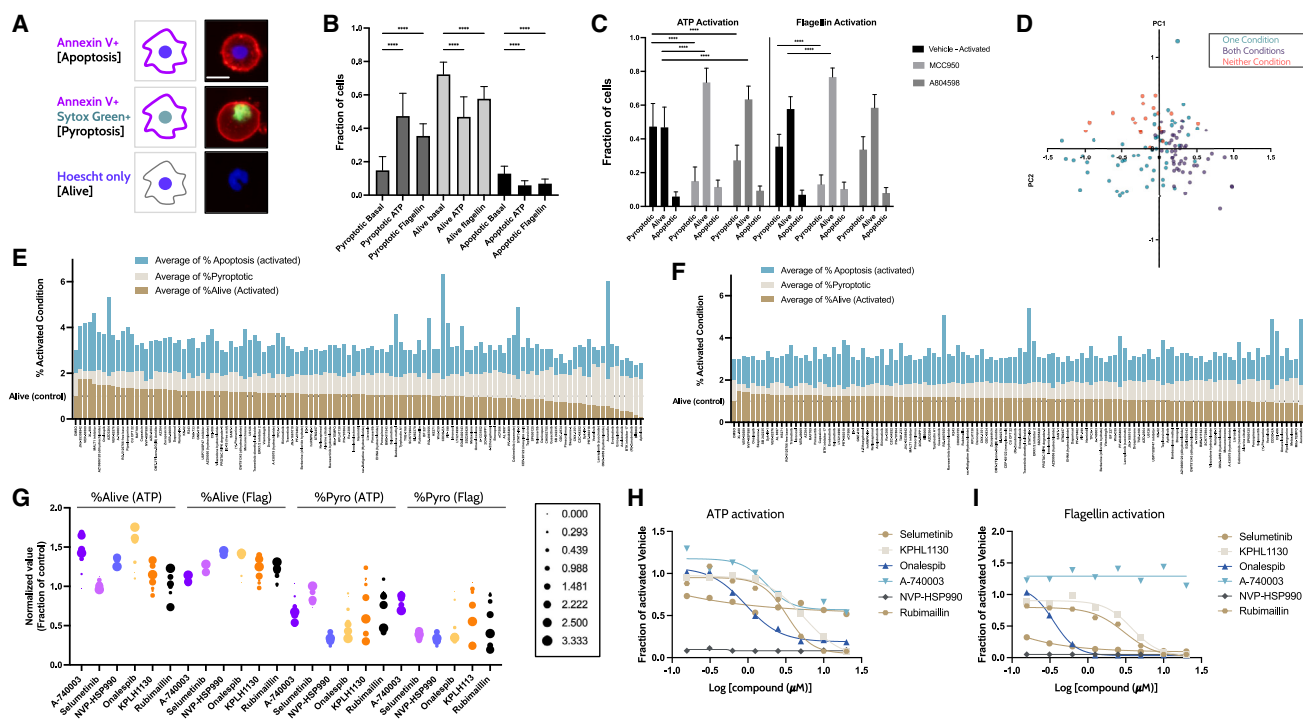
Figure 7. Orthogonal validation of compounds belonging to different mechanistic classes in primary human monocytes

(A) Staining schematic for death classifications. Apoptotic cells flip the negatively charged lipid phosphatidylserine to the outer leaflet, where Annexin V can bind. Pyroptotic/necrotic cells with compromised plasma membranes allow Annexin V and SYTOX green to enter the cells and bind intracellular phosphatidylserine. Supervised classifiers were trained to identify three death associated classes: (1) healthy/alive (Annexin V⁻ SYTOX green⁻ cells), (2) apoptotic (Annexin V⁺ SYTOX green⁻), and (3) pyroptotic (Annexin V⁺/⁻ SYTOX green⁺). Scale bar, 10 μm.

(B) Performance of death classes by condition. Shown as average with standard deviation of the fraction of cells of all replicates across 4 experiments. Minimum of 96 replicates per experiment for activation conditions and 20 replicates per experiment of the DMSO basal control. Statistical significance measured by two-tailed unpaired Mann Whitney u-test; ****$p < 0.0001$.

(C) Performance of control inhibitors on death classes by condition. Shown as average with standard deviation of the fraction of cells of all replicates across 4 experiments. 6 replicates per concentration for compounds and 20 replicates per experiment of the DMSO basal control. Statistical significance determined by two-tailed unpaired Mann Whitney u-test, as indicated. *$p < 0.05$.

(D) PCA of compounds using values of their average effects on % alive (basal), % alive (activated), and % pyroptotic. Colored according to categorizations of both (ATP and flagellin), neither, or single condition inhibitors using criteria for each condition of: increase in % alive cells, >50% decrease in pyroptotic cells, and >30% decrease in IL-1β, relative to the activated vehicle control.

(E) Compound-mediated effects on median number of pyroptotic, apoptotic, and alive cells under ATP activation; average fraction of cells of 3 replicates for each of 7 concentrations per compound normalized to vehicle controls for basal state or activated state (DMSO). Shown as fraction of the total for each treatment condition.

(F) Same as E, but under flagellin activation.

(G) Top inhibitors effects on alive and pyroptotic cells relative to controls under ATP or Flagellin activation (specified in figure). Each point on the graph is the average of 6 replicates. Compound concentrations vary by the size of the points (legend) to visualize dose-dependent responses.

(H) Compound mediated inhibition of IL-1β following ATP activation. Plotted as average of 6 replicates over a 7 point titration curve, fit using a log (agonist) vs. response variable slope (four parameters) least squares fit model.

(I) Same as H, but with flagellin activation. See also Figures S8, S9, Tables S5 and Table S6.

DISCUSSION

Dysregulation of inflammasome pathways has been linked to a multitude of human diseases that range widely in severity and onset, but how these interconnected pathways contribute to varying pathologies is largely handicapped by single-readout assays. Clinical pipelines may benefit from discovery programs that focus on aligning mechanistically distinct therapeutics with the diversity of relevant disease states. For example, compounds that act on early pathway targets may be ideal for treating chronic indications such as gout where tolerability and general inflammatory inhibition

must be considered, while broad-acting, late pathway inhibitors may be necessary to abrogate widespread inflammation in acute indications such as sepsis.

Traditional methods for studying inflammasome activation and drug discovery are limited in their ability to resolve mechanistic differences between conditions. In order to acquire as much physiologically relevant data as possible at the single cell level, we therefore designed a scalable *in vitro* imaging system in human PBMCs stained with a palette of cell biological dyes and treated with a series of control modulators to capture cells at all stages between the basal and pyroptotic states.
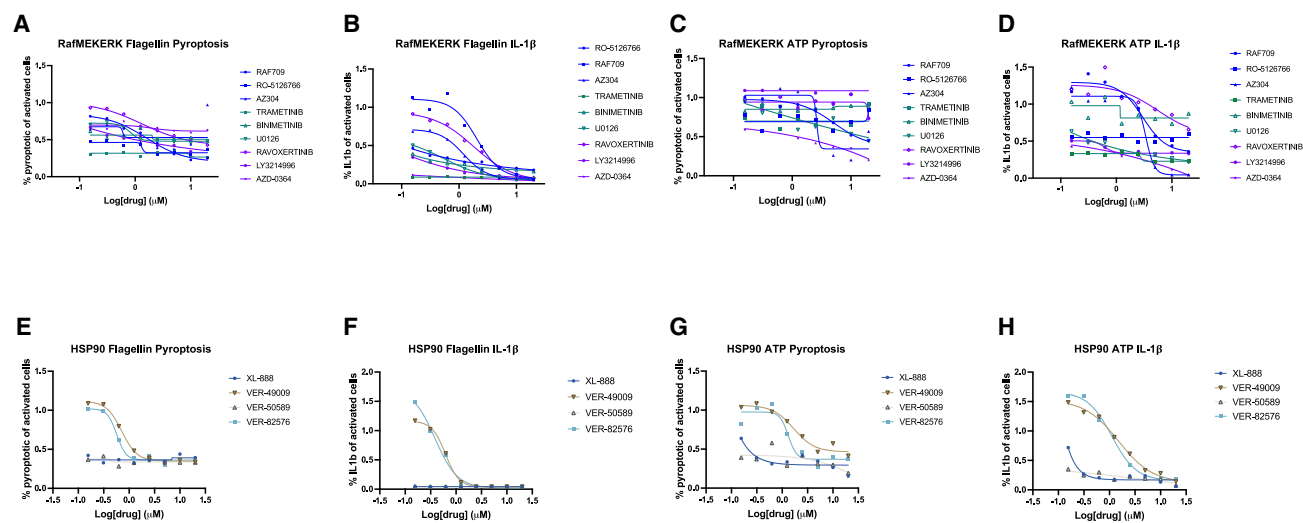
Figure 8. Raf, MEK, ERK, and HSP90 inhibitors effectively block inflammasome signaling in human monocytes

(A) Pyroptosis inhibition curves of three inhibitors targeted at each of Raf (blue), MEK (teal), and ERK (purple) on flagellin activated human monocytes. Plotted as average of 3 replicates over a 7 point titration curve, fit using a log (agonist) vs. response variable slope (four parameters) least squares fit model.

(B) IL-1β inhibition curves of three inhibitors targeted at each of Raf (blue), MEK (teal), and ERK (purple) activated human monocytes. Plotted as average of 6 replicates over a 7 point titration curve, fit using a log (agonist) vs. response variable slope (four parameters) least squares fit model.

(C) Same as A, but on ATP activated monocytes.

(D) Same as B, but on ATP activated monocytes.

(E) Pyroptosis inhibition curves of three HSP90 inhibitors on flagellin activated human monocytes. Plotted as average of 3 replicates over a 7 point titration curve, fit using a log(agonist) vs. response variable slope (four parameters) least squares fit model.

(F) IL-1β inhibition curves of three HSP90 inhibitors on flagellin activated human monocytes. Plotted as average of 6 replicates over a 7 point titration curve, fit using a log(agonist) vs. response variable slope (four parameters) least squares fit model.

(G) Same as C but on ATP activated monocytes.

(H) Same as D, but on ATP activated monocytes.

This experimental approach built off the principles of cell painting, which have facilitated automated quantification of agnostic features from HCI datasets, and integrated fluorescence microscopy into scalable, high-throughput work-flows.[36] While this foundational methodology has revolutionized phenotypic screening, it often has limited biological interpretability. We therefore developed a combined ML and cell biology-based analytical approach that utilizes high-dimensional image embeddings extracted from high-content imaging data using pretrained convolutional neural networks.

To build our analytical toolkit, we first trained classifiers to recognize various degrees of inflammasome activation and inhibition from images of cells challenged with established compound modulators. We used the resulting outputs to predict compound-mediated effects from HCI data. Additionally, we calculated on- and off-basis projection values to determine whether compound-mediated effects fell along an expected axis or forced cells into unique states, and applied unsupervised hierarchical clustering to discover PDCS with statistical associations to basal, activated, or inhibited states. All of these readouts were validated using ground-truth measurements for ASC speck formation and literature-established inflammasome control conditions. Importantly, ASC speck validation largely precludes our readouts from being confounded by contributions by alternative inflammasome pathways that do not require ASC, but nonetheless these pathways may be activated in our assays.[37]

It is necessary to note that no single analytical method was able to fully disambiguate inflammasome cellular states. For example, trained classifiers were used to predict compound-mediated effects relative to the activated states, but under the direct ATP activation condition, downstream inhibitors resembled the activated state due to relatively low signal propagation. Inhibited cells could be resolved from activated ones, however, by our TS method that aggregated automated ASC speck quantifications, projection scores, frequency of PDCSs, and trained classifier scores for all activation and inhibition conditions.

As a parallel process for the discovery and mechanistic classification of inhibitors directly in the deep learning representation space, we also developed the CMDS of morphological profiles method. Contrary to targeted strategies, this approach does not require specific controls in order to identify hits or conditions, and therefore is largely agnostic to biological systems. CMDS importantly validated the majority of TSCC-surfaced compounds in an unbiased, hypothesis-independent manner.

Altogether, we generated profiles of mechanistically distinct inflammasome states that ranged from basal to pyroptotic and which were used to define compound mechanisms of action in a bioactive compound screen. Through this process, we validated and characterized many literature-established inflammasome modulators that were part of the screening library, and which importantly served as internal controls for our methods. Further, we identified many instances where multiple compounds that were annotated to act on the same target were

surfaced as hits and assigned to the same mechanistic class, implicating their respective targets in inflammasome signaling.

Such target identification led to the discovery that the Raf-MEK-ERK pathway, including the Raf chaperone HSP90, plays a vital role in inflammasome signaling. While ERK and HSP90 have been previously linked to inflammasome signaling[38,39] and NLRP3,[30,40] to our knowledge this is the first study to identify and mechanistically classify these interacting proteins in parallel as inflammasome modulators.

In PBMCs, compounds targeting this pathway restore activated cells to their basal states rather than suspending them in downstream stressed and activated states, while in primary monocytes, they consistently and potently inhibit pyroptosis without shifting cells toward a non-inflammatory apoptotic cell death. Altogether we identified, validated, and mechanistically characterized 34 compounds targeting the Raf pathway as inflammasome modulators across a series of orthogonal experiments and an array of established and unbiased readouts. Aggregating individual compound data from this pathway into target specific groups for ERK, MEK, Raf, and HSP90 generally indicates that they are involved downstream of an early convergence point of multiple activators, and upstream of gasdermin D pore formation and signal amplification. This could support a role for the Raf pathway modulating complex formation by acting on a common component of the inflammasome complexes like ASC or a recruitment signal.

Importantly, the discovery and validation of a multitude of compounds targeting each of several proteins along this signaling pathway simultaneously cross-validate each of their independent roles, and also identify the Raf pathway as a potentially rich source of therapeutic targets for inflammasome related pathologies.

More generally, this approach could be applied to any set of complex, interconnected biological pathways to identify a spectrum of mechanistically distinct cellular states associated with activation, inhibition, health, or dysregulation, which in turn could drive multiple target or drug discovery programs forward from a single screen.

Limitations of the study

The data presented here, while physiologically relevant and derived from human primary cells, are limited in their ability to capture the full complexity and variability of an *in vivo* biological system. Additionally, while our experiments distributed every donor across every condition, so effects associated with age, ethnicity, and gender were minimized, the majority of commercially available human primary cells (PBMCs and monocytes) were isolated from Caucasian males. Thus, there may be limitations when extrapolating data to cells from donors of different genders and ethnicities.

Given the nature of unbiased image embeddings extracted using neural networks, there are limits in being able to comprehensively describe the respective image features used in model training.

We utilized a large panel of small molecules for mechanistic analysis of Raf pathway inhibitors and focused on the average effects of multiple compounds for each target in the pathway. We cannot exclude the possibility that some of these compounds mediate off-target effects, and this should be considered in future studies to further clarify the mechanisms of action of Raf pathway involvement in inflammasome signaling.

RESOURCE AVAILABILITY

Lead contact

Further information and requests for resources and reagents should be directed to and will be fulfilled by the lead contact, Rachel DeVay Jacobson (rachelmarie804@gmail.com).

Materials availability

This study did not generate new unique reagents

Data and code availability

- All training datasets, images, and model outputs are available in this Spring platform and are publicly available as of the date of publication. Link provided in the key resources table.
- Image embeddings and original code for models have been deposited at Zenodo and are publicly available as of the date of publication. Link provided in the key resources table.
- Any additional information required to reanalyze the data reported in this paper is available from the lead contact upon request.

STAR★METHODS

Detailed methods are provided in the online version of this paper and include the following:

- KEY RESOURCES TABLE
- EXPERIMENTAL MODEL AND STUDY PARTICIPANT DETAILS
  - Cell lines and primary cells
- METHOD DETAILS
  - Compound preparation
  - Cell thawing and plating
  - Cell fixation and staining
  - Functional assays
  - Readouts
  - Computational methods
- QUANTIFICATION AND STATISTICAL ANALYSIS

- ○ Titration curves and IC50 determination
- ○ Statistical significance between groups
- ○ Principal component analysis (PCA)
- ○ Statistical measurements from computational analyses

SUPPLEMENTAL INFORMATION

Supplemental information can be found online at https://doi.org/10.1016/j.isci.2024.111404.

REFERENCES

1. Kastbom, A., Verma, D., Eriksson, P., Skogh, T., Wingren, G., and Söderkvist, P. (2008). Genetic variation in proteins of the cryopyrin inflammasome influences susceptibility and severity of rheumatoid arthritis (The Swedish TIRA project). Rheumatology *47*, 415–417. https://doi.org/10.1093/rheumatology/kem372.

2. Miao, Z.-M., Zhao, S.-H., Yan, S.-L., Li, C.-G., Wang, Y.-G., Meng, D.-M., Zhou, L., and Mi, Q.-S. (2009). NALP3 inflammasome functional polymorphisms and gout susceptibility. Cell Cycle *8*, 27–30. https://doi.org/10.4161/cc.8.1.7325.

3. Danielski, L.G., Giustina, A.D., Bonfante, S., Barichello, T., and Petronilho, F. (2020). The NLRP3 Inflammasome and Its Role in Sepsis Development. Inflammation *43*, 24–31. https://doi.org/10.1007/s10753-019-01124-9.

4. McVey, M.J., Steinberg, B.E., and Goldenberg, N.M. (2021). Inflammasome activation in acute lung injury. Am. J. Physiol. Lung Cell Mol. Physiol. *320*, L165–L178. https://doi.org/10.1152/ajplung.00303.2020.

5. Sharma, D., and Kanneganti, T.-D. (2016). The cell biology of inflammasomes: Mechanisms of inflammasome activation and regulation. J. Cell Biol. *213*, 617–629. https://doi.org/10.1083/jcb.201602089.

6. Bergsbaken, T., Fink, S.L., and Cookson, B.T. (2009). Pyroptosis: host cell death and inflammation. Nat. Rev. Microbiol. *7*, 99–109. https://doi.org/10.1038/nrmicro2070.

7. Toldo, S., Mauro, A.G., Cutter, Z., and Abbate, A. (2018). Inflammasome, pyroptosis, and cytokines in myocardial ischemia-reperfusion injury. Am. J. Physiol. Heart Circ. Physiol. *315*, H1553–H1568. https://doi.org/10.1152/ajpheart.00158.2018.

8. Jo, E.-K., Kim, J.K., Shin, D.-M., and Sasakawa, C. (2016). Molecular mechanisms regulating NLRP3 inflammasome activation. Cell. Mol. Immunol. *13*, 148–159. https://doi.org/10.1038/cmi.2015.95.

9. Sborgi, L., Rühl, S., Mulvihill, E., Pipercevic, J., Heilig, R., Stahlberg, H., Farady, C.J., Müller, D.J., Broz, P., and Hiller, S. (2016). GSDMD membrane pore formation constitutes the mechanism of pyroptotic cell death. EMBO J. *35*, 1766–1778. https://doi.org/10.15252/embj.201694696.

10. Broz, P., and Dixit, V.M. (2016). Inflammasomes: mechanism of assembly, regulation and signalling. Nat. Rev. Immunol. *16*, 407–420. https://doi.org/10.1038/nri.2016.58.

11. Bray, M.-A., Singh, S., Han, H., Davis, C.T., Borgeson, B., Hartland, C., Kost-Alimova, M., Gustafsdottir, S.M., Gibson, C.C., and Carpenter, A.E. (2016). Cell Painting, a high-content image-based assay for morphological profiling using multiplexed fluorescent dyes. Nat. Protoc. *11*, 1757–1774. https://doi.org/10.1038/nprot.2016.105.

12. Hu, J.J., Liu, X., Xia, S., Zhang, Z., Zhang, Y., Zhao, J., Ruan, J., Luo, X., Lou, X., Bai, Y., et al. (2020). FDA-approved disulfiram inhibits pyroptosis by blocking gasdermin D pore formation. Nat. Immunol. *21*, 736–745. https://doi.org/10.1038/s41590-020-0669-6.

13. Coll, R.C., Hill, J.R., Day, C.J., Zamoshnikova, A., Boucher, D., Massey, N.L., Chitty, J.L., Fraser, J.A., Jennings, M.P., Robertson, A.A.B., and Schroder, K. (2019). MCC950 directly targets the NLRP3 ATP-hydrolysis

14. Zhao, Y., Yang, J., Shi, J., Gong, Y.-N., Lu, Q., Xu, H., Liu, L., and Shao, F. (2011). The NLRC4 inflammasome receptors for bacterial flagellin and type III secretion apparatus. Nature *477*, 596–600. https://doi.org/10.1038/nature10510.

15. Dos Reis, E.C., Leal, V.N.C., Soares, J.L.d.S., Fernandes, F.P., Souza de Lima, D., de Alencar, B.C., and Pontillo, A. (2019). Flagellin/NLRC4 Pathway Rescues NLRP3-Inflammasome Defect in Dendritic Cells From HIV-Infected Patients: Perspective for New Adjuvant in Immunocompromised Individuals. Front. Immunol. *10*, 1291. https://doi.org/10.3389/fimmu.2019.01291.

16. Gram, A.M., Wright, J.A., Pickering, R.J., Lam, N.L., Booty, L.M., Webster, S.J., and Bryant, C.E. (2021). Salmonella Flagellin Activates NAIP/NLRC4 and Canonical NLRP3 Inflammasomes in Human Macrophages. J. Immunol. *206*, 631–640. https://doi.org/10.4049/jimmunol.2000382.

17. Man, S.M., Hopkins, L.J., Nugent, E., Cox, S., Glück, I.M., Tourlomousis, P., Wright, J.A., Cicuta, P., Monie, T.P., and Bryant, C.E. (2014). Inflammasome activation causes dual recruitment of NLRC4 and NLRP3 to the same macromolecular complex. Proc. Natl. Acad. Sci. USA *111*, 7403–7408. https://doi.org/10.1073/pnas.1402911111.

18. Lee, S.I., Kang, S.K., Jung, H.J., Chun, Y.H., Kwon, Y.D., and Kim, E.C. (2015). Muramyl dipeptide activates human beta defensin 2 and pro-inflammatory mediators through Toll-like receptors and NLRP3 inflammasomes in human dental pulp cells. Clin. Oral Invest. *19*, 1419–1428.

19. Nagar, A., DeMarco, R.A., and Harton, J.A. (2019). Inflammasome and Caspase-1 Activity Characterization and Evaluation: An Imaging Flow Cytometer–Based Detection and Assessment of Inflammasome Specks and Caspase-1 Activation. J. Immunol. *202*, 1003–1015. https://doi.org/10.4049/jimmunol.1800973.

20. Wang, Y., Yang, C., Mao, K., Chen, S., Meng, G., and Sun, B. (2013). Cellular localization of NLRP3 inflammasome. Protein Cell *4*, 425–431. https://doi.org/10.1007/s13238-013-2113-2.

21. Stirling, D.R., Swain-Bowden, M.J., Lucas, A.M., Carpenter, A.E., Cimini, B.A., and Goodman, A. (2021). CellProfiler 4: improvements in speed, utility and usability. BMC Bioinf. *22*, 433. https://doi.org/10.1186/s12859-021-04344-9.

22. White, B., Komalo, B., Nicolaisen, L., Donne, M., Marsh, C., DeVay, R.M., Nguyen, A.M., Cousin, W., Heinrich, J., Van Trump, W.J., et al. (2020). A Multi-Phenotype System to Discover Therapies for Age-Related Dysregulation of the Immune Response to Viral Infections. Preprint at bioRxiv. https://doi.org/10.1101/2020.07.30.223875.

23. Chen, X., He, W.T., Hu, L., Li, J., Fang, Y., Wang, X., Xu, X., Wang, Z., Huang, K., and Han, J. (2016). Pyroptosis is driven by non-selective gasdermin-D pore and its morphology is different from MLKL channel-mediated necroptosis. Cell Res. *26*, 1007–1020. https://doi.org/10.1038/cr.2016.100.

24. McInnes, L., Healy, J., Saul, N., and Großberger, L. (2018). UMAP: Uniform Manifold Approximation and Projection. J. Open Source Softw. *3*, 861. https://doi.org/10.21105/joss.00861.

25. Moffat, J.G., Vincent, F., Lee, J.A., Eder, J., and Prunotto, M. (2017). Opportunities and challenges in phenotypic drug discovery: an industry perspective. Nat. Rev. Drug Discov. *16*, 531–543. https://doi.org/10.1038/nrd.2017.111.

26. Jiang, H., He, H., Chen, Y., Huang, W., Cheng, J., Ye, J., Wang, A., Tao, J., Wang, C., Liu, Q., et al. (2017). Identification of a selective and direct NLRP3 inhibitor to treat inflammatory disorders. J. Exp. Med. *214*, 3219–3238. https://doi.org/10.1084/jem.20171419.

27. Fowler, B.J., Gelfand, B.D., Kim, Y., Kerur, N., Tarallo, V., Hirano, Y., Amarnath, S., Fowler, D.H., Radwan, M., Young, M.T., et al. (2014). Nucleoside reverse transcriptase inhibitors possess intrinsic anti-inflammatory activity. Science *346*, 1000–1003. https://doi.org/10.1126/science.1261754.

28. Nizami, S., Millar, V., Arunasalam, K., Zarganes-Tzitzikas, T., Brough, D., Tresadern, G., Brennan, P.E., Davis, J.B., Ebner, D., and Di Daniel, E. (2021). A phenotypic high-content, high-throughput screen identifies inhibitors of NLRP3 inflammasome activation. Sci. Rep. *11*, 15319. https://doi.org/10.1038/s41598-021-94850-w.

29. Ambati, J., Magagnoli, J., Leung, H., Wang, S.B., Andrews, C.A., Fu, D., Pandey, A., Sahu, S., Narendran, S., Hirahara, S., et al. (2020). Repurposing anti-inflammasome NRTIs for improving insulin sensitivity and reducing type 2 diabetes development. Nat. Commun. *11*, 4737. https://doi.org/10.1038/s41467-020-18528-z.

30. Nizami, S., Arunasalam, K., Green, J., Cook, J., Lawrence, C.B., Zarganes-Tzitzikas, T., Davis, J.B., Di Daniel, E., and Brough, D. (2021). Inhibition of the NLRP3 inflammasome by HSP90 inhibitors. Immunology *162*, 84–91. https://doi.org/10.1111/imm.13267.

31. Meyers, A.K., Wang, Z., Han, W., Zhao, Q., Zabalawi, M., Duan, L., Liu, J., Zhang, Q., Manne, R.K., Lorenzo, F., et al. (2023). Pyruvate dehydrogenase kinase supports macrophage NLRP3 inflammasome activation during acute inflammation. Cell Rep. *42*, 111941. https://doi.org/10.1016/j.celrep.2022.111941.

32. Ito, M., Shichita, T., Okada, M., Komine, R., Noguchi, Y., Yoshimura, A., and Morita, R. (2015). Bruton's tyrosine kinase is essential for NLRP3 inflammasome activation and contributes to ischaemic brain injury. Nat. Commun. *6*, 7360. https://doi.org/10.1038/ncomms8360.

33. McCubrey, J.A., Steelman, L.S., Chappell, W.H., Abrams, S.L., Wong, E.W.T., Chang, F., Lehmann, B., Terrian, D.M., Milella, M., Tafuri, A., et al. (2007). Roles of the Raf/MEK/ERK pathway in cell growth, malignant transformation and drug resistance. Biochim. Biophys. Acta *1773*, 1263–1284. https://doi.org/10.1016/j.bbamcr.2006.10.001.

34. Grbovic, O.M., Basso, A.D., Sawai, A., Ye, Q., Friedlander, P., Solit, D., and Rosen, N. (2006). V600E B-Raf requires the Hsp90 chaperone for stability and is degraded in response to Hsp90 inhibitors. Proc. Natl. Acad. Sci. USA *103*, 57–62. https://doi.org/10.1073/pnas.0609973103.

35. Han, J., Kamber, M., and Pei, J. (2012). Data Mining (Third Edition). 39–82. https://doi.org/10.1016/b978-0-12-381479-1.00002-2.

36. Wawer, M.J., Li, K., Gustafsdottir, S.M., Ljosa, V., Bodycombe, N.E., Marton, M.A., Sokolnicki, K.L., Bray, M.-A., Kemp, M.M., Winchester, E., et al. (2014). Toward performance-diverse small-molecule libraries for cell-based phenotypic screening using multiplexed high-dimensional profiling.

37. Gaidt, M.M., Ebert, T.S., Chauhan, D., Schmidt, T., Schmid-Burgk, J.L., Rapino, F., Robertson, A.A.B., Cooper, M.A., Graf, T., and Hornung, V. (2016). Human Monocytes Engage an Alternative Inflammasome Pathway. Immunity *44*, 833–846. https://doi.org/10.1016/j.immuni.2016.01.012.

38. Ghonime, M.G., Shamaa, O.R., Das, S., Eldomany, R.A., Fernandes-Alnemri, T., Alnemri, E.S., Gavrilin, M.A., and Wewers, M.D. (2014). Inflammasome Priming by Lipopolysaccharide Is Dependent upon ERK Signaling and Proteasome Function. J. Immunol. *192*, 3881–3888. https://doi.org/10.4049/jimmunol.1301974.

39. Peng, Q., Yin, R., Zhu, X., Jin, L., Wang, J., Pan, X., and Ma, A. (2022). miR-155 activates the NLRP3 inflammasome by regulating the MEK/ERK/NF-κB pathway in carotid atherosclerotic plaques in ApoE−/− mice. J. Physiol. Biochem. *78*, 365–375. https://doi.org/10.1007/s13105-022-00871-y.

40. Shi, W., Xu, G., Zhan, X., Gao, Y., Wang, Z., Fu, S., Qin, N., Hou, X., Ai, Y., Wang, C., et al. (2020). Carnosol inhibits inflammasome activation by directly targeting HSP90 to treat inflammasome-mediated diseases. Cell Death Dis. *11*, 252. https://doi.org/10.1038/s41419-020-2460-x.

41. Dagher, M., Ongo, G., Robichaud, N., Kong, J., Rho, W., Teahulos, I., Tavakoli, A., Bovaird, S., Merjaneh, S., Tan, A., et al. (2023). nELISA: A high-throughput, high-plex platform enables quantitative profiling of the secretome. Preprint at bioRxiv. https://doi.org/10.1101/2023.04.17.535914.

42. Simonyan, K., and Zisserman, A. (2014). Very Deep Convolutional Networks for Large-Scale Image Recognition. Preprint at arXiv. https://doi.org/10.4850/arXiv.1409.1556.

43. Tan, M., and Le, Q.V. (2021). EfficientNetV2: Smaller Models and Faster Training. Preprint at arXiv. https://doi.org/10.48550/arXiv.2104.00298.

44. Krishnapuram, B., Shah, M., Smola, A., Aggarwal, C., Shen, D., Rastogi, R., Chen, T., and Guestrin, C. (2016). XGBoost. In Proc. 22nd ACM SIGKDD Int. Conf. Knowl. Discov. Data Min., pp. 785–794. https://doi.org/10.1145/2939672.2939785.

45. van der Walt, S., Schönberger, J.L., Nunez-Iglesias, J., Boulogne, F., Warner, J.D., Yager, N., Gouillart, E., and Yu, T.; scikit-image contributors (2014). scikit-image: image processing in Python. PeerJ *2*, e453. https://doi.org/10.7717/peerj.453.

Proc. Natl. Acad. Sci. USA *111*, 10911–10916. https://doi.org/10.1073/pnas.1410933111.

STAR★METHODS

KEY RESOURCES TABLE

REAGENT or RESOURCE	SOURCE	IDENTIFIER
Antibodies		
anti-ASC rabbit pAb	Adipogen AG-25B-0006-C100	RRID: AB_11181932
Goat anti-rabbit 647 secondary antibody	Thermo A-21245	RRID: AB_2535813
Biological samples		
Cryopreserved human PBMCs	iXCells Biotechnology	10HU-003-CR10M, 10HU-003-CR100M
Cryopreserved human primary monocytes	iXCells Biotechnology	10HU-008N-10M
Chemicals, peptides, and recombinant proteins		
RPMI 1640	Gibco	21870092
HEPES	Thermo	15630080
Penicillin and Streptomycin	Thermo	15140163
L-glutathione	Thermo	25030081
Sodium pyruvate	Sigma	S8636-100ML
Vitamins	Sigma	M6895-100ML
Non-essential amino acids	Sigma	M7145-100ML
beta-mercaptoethanol	Thermo	31350010
FBS (heat inactivated)	Thermo	10437036
Bovine Growth Serum	HyClone	AB10180149
Bioactive screening libraries	MedChemExpress	HY-L001, HY-L001P
DMSO	Sigma	d2650
LPS	Invivogen	tlrl-eklps
Nigericin	Invivogen	tlrl-nig
Poly(I:C)	Invivogen	vac-pic
Flagellin (S. typhimurium)	Invivogen	tlrl-stfla
ATP	Thermo	R0441
MDP	Bachem	4009623
Staurosporine	R&D Systems	1285
Digoxin	Cayman Chem	22266
Elesclomol	SelleckChem	S1052
Lanatoside C	MedChemExpress	HY-B1030
Darapladib	SelleckChem	S7520
Doxorubicin	SelleckChem	S1208
Annexin V	AbCam	ab14150
SYTOX green	Promega	S7020
Concanavalin A Alexa Fluor 488	Thermo	C11252
Phalloidin Phenovue Fluor 568	Perkin Elmer	CP25681
Hoechst 33342	Thermo	H3570
Paraformaldehyde	EMS	15710-S
Critical commercial assays		
Fireplex assay	Abcam	ab234897
Deposited data		
Image embeddings and original code for models	Zenodo	https://doi.org/10.5281/zenodo.13694396
Spring Inflammasome Benchmark Dataset	GitHub	https://github.com/spring-discovery/inflammasome-benchmark-dataset

(Continued on next page)

Continued

REAGENT or RESOURCE	SOURCE	IDENTIFIER
All training datasets, images, and model outputs. All data are downloadable (image files and .csv files of data, features, and analyses)	Spring Webapp	https://tinyurl.com/InflammasomeChenetal
Experimental models: Cell lines		
THP1-HMGB1-Lucia™ cells	Invivogen	Thp0gb1lc; RRID:CVCL_A8BE
Software and algorithms		
GraphPad Prism		RRID:SCR_002798
Excel		RRID:SCR_016137
Spring AI Software		
Other		
HeraCell VIOS 160i normoxic incubator	ThermoFisher Scientific	51030403
Echo 650 Liquid Handler	Beckman Coulter	
Microlab Star liquid handler	Hamilton	RRID:SCR_019993
Biotek EL406	Agilent	RRID:SCR_019735
ImageXpress Micro Confocal high content imager	Molecular Devices	RRID:SCR_020294
Mantis	Formulatrix	RRID:SCR_019923

EXPERIMENTAL MODEL AND STUDY PARTICIPANT DETAILS

Cell lines and primary cells
Human PBMCs
Isolated cells from male and female donors aged 45–55 were acquired commercially from iXCells Biotechnology (10HU-003-CR10M, 10HU-003-CR100M). The majority of cells were isolated from Caucasian males. Cells were verified by iXCells to be free of mycoplasma, other bacteria, yeast, fungi, HIV, HBV, and HCV.

Donor samples were not separated into different experimental groups. Cells from each donor were distributed evenly across experimental conditions, so gender, ethnicity, and age of donors did not influence the outcomes of our analyses. The number of donors run per experiment are detailed in the figure legends. There may be limitations when extrapolating data to cells from donors of different genders and ethnicities.

Cryopreserved primary human PBMCs were cultured in RPMI 1640 supplemented with 2mM glutamine, 25 mM HEPES, pen/strep, 1 mM sodium pyruvate, 1x vitamins, 1x non-essential amino acids, 50 μM beta-mercaptoethanol), and 10% heat-inactivated fetal bovine serum. Random samples were periodically tested and found to be mycoplasma-free.

Human monocytes
Isolated cells from male and female donors aged 45–55 were acquired commercially from iXCells Biotechnology (10HU-008*N*-10M). The majority of cells were isolated from Caucasian males. Cells were verified by iXCells to be free of mycoplasma, other bacteria, yeast, fungi, HIV, HBV, and HCV.

Donor samples were not separated into different experimental groups. Cells from each donor were distributed evenly across experimental conditions, so gender, ethnicity, and age of donors did not influence the outcomes of our analyses. The number of donors run per experiment are detailed in the figure legends. There may be limitations when extrapolating data to cells from donors of different genders and ethnicities.

Cryopreserved primary human monocytes were cultured in RPMI 1640 supplemented with 2mM glutamine, 25 mM HEPES, pen/strep, 1 mM sodium pyruvate, 1x vitamins, 1x non-essential amino acids, 50 μM beta-mercaptoethanol), and 10% heat-inactivated fetal bovine serum.

Cell lines
THP1-HMGB1-Lucia cells (Invivogen, thp0gb1lc, RRID:CVCL_A8BE). These cells were purchased directly from Invivogen and guaranteed to be mycoplasma free. THP1 cells are derived from monocytes isolated from a 1-year old male with acute monocytic leukemia.

THP1-HMGB1-Lucia cells were cultured in RPMI 1640 supplemented with 2 mM L-glutamine, 25 mM HEPES, 10% heat-inactivated fetal bovine serum, 1 μg/mL Normocin, and pen/strep, according to manufacturer's recommendations.

Cells were cultured in a humidified HeraCell VIOS 160i normoxic incubator (ThermoFisher Scientific, 51030403) at 37C and 5% CO_2.

METHOD DETAILS

Compound preparation

For inflammasome inhibitor compound preparation, an Echo 650 Liquid Handler (Beckman Coulter) was used to prepare compound matrices on 384-well plates (Labcyte, PP-02200). Compounds were sourced from MedChemExpress bioactive screening libraries (HY-L001, HY-L001P). The volume of DMSO in each well was normalized to achieve 0.5% final DMSO assay concentration. The compound plates were stored at 4C in the dark overnight prior to use in assays.

Inflammasome activator compounds were prepped at 10x the concentrations described in the assay methods below in serum-free media.

Cell thawing and plating

On the day of experimentation, cells were thawed and washed 2x in PBMC media (RPMI 1640 w/2mM glutamine, 25 mM HEPES, pen/strep, 1 mM sodium pyruvate, 1x vitamins, 1x non-essential amino acids, 50 μM beta-mercaptoethanol) with 10% FBS before resuspending in serum-free media (PBMC media without FBS) prior to plating. Washing consisted of centrifuging the cells at 300g for 10 min, then aspirating and resuspending in media.

Cell fixation and staining
Cell fixing and permeabilizing
Prior to staining, the PBMCs were fixed by adding 16% PFA with the Microlab Star liquid handler (Hamilton; RRID:SCR_019993) to bring the final concentration to 4% PFA, for 15 min at room temperature. The cells were then washed 3x with staining buffer (1% bovine growth serum in PBS), and permeabilized with 0.3% Triton X- and 1% bovine growth serum in PBS for 15 min at room temperature. The cells were then washed 3x again with staining buffer. All washing and permeabilization steps were done on a Biotek EL406 (Agilent; RRID:SCR_019735).

Immunofluorescence ASC specks
After fixing and permeabilization, the PBMCs were stained with anti-ASC rabbit pAb (AL177, Adipogen AG-25B-0006-C100; RRID:AB_11181932) at 25 μg/mL in staining buffer (1% bovine growth serum in PBS) along with Cell Painting dyes, overnight at 4C. The cells were then washed 3x with staining buffer, and stained with Goat anti-rabbit 647 secondary antibody (Thermo A-21245; RRID:AB_2535813) at 1 μg/mL in staining buffer for 1 h at room temperature. Finally, cells were washed 3x with PBS. All washing and staining steps were done on a Biotek EL406 (Agilent).

Cell staining
After fixing and permeabilization, cells were stained with Concanavalin A Alexa Fluor 488 (Thermo C11252) at 25 μg/mL and Phalloidin Phenovue Fluor 568 (PerkinElmer CP25681) at 66 nM in staining buffer (1% bovine growth serum in PBS) along with anti-ASC antibody, overnight at 4C. The cells were then washed 3x with staining buffer, and stained with Goat anti-rabbit 647 secondary antibody (Thermo A-21245) at 1 μg/mL in staining buffer for 1 h at room temperature. Finally, the cells were washed 3x in PBS, stained with Hoechst 33342 (Thermo) at 0.2 μg/mL in PBS for 15 min, then washed again 3x in PBS. All washing and staining steps were done on a Biotek EL406 (Agilent).

Functional assays
Inflammasome inhibition
Inflammasome inhibitor compounds prepped at 10x concentration in serum-free media were then added using the Microlab Star liquid handler to bring the final compound concentration to 1x. Cells were incubated with inhibitor compounds for 30 min at 37C. prior to Inflammasome activator compound addition.

Inflammasome activation (PBMCs)
A Microlab Star liquid handler (Hamilton) was used to plate cryopreserved primary human PBMCs (iXCells) on 384-well imaging plates (Greiner 781091). Cells in serum-free media were seeded at a density of 15,000 cells per well. After a 10 min room temperature incubation and a 30 min incubation at 37C, PBMC media with 50% FBS was added to bring FBS to 10% final concentration.

Inflammasome activator compounds were added using a Mantis (Formulatrix; RRID:SCR_019923) to the PBMCs and incubated for 4 h at 37C before fixing and staining. Activators included LPS (0.1 μg/mL), Nigericin (20μM), Poly(I:C) (20μg/mL), Flagellin (1 μg/mL), ATP (1mM), and MDP (10μg/mL). A schematic of the order of addition for this assay is shown in Figure S10.

Death classification and pyroptosis assays (primary human monocytes)
Primary human monocytes (iXCells) were thawed and plated in 384-well imaging plates (Greiner, 781091) at 10,000 cells/well in serum-free media to allow for attachment to the plate. Cells were allowed to settle for 10 min at room temperature and then incubated at 37°C for 30 min before fetal bovine serum (Thermo, 26140-079) was added to a final concentration of 10%. Compounds (concentrations indicated in figures) were then added using a Microlab Star liquid handler (Hamilton).

For monocyte activation, 0.1 μg/mL LPS priming for 4 h followed by a 2 h activation with ATP (1 mM final) or Nigericin (20 μM). Non-LPS primed conditions were incubated for 6 h with the same concentrations of ATP or nigericin, or alternatively with 1 μg/mL Flagellin. Supernatants were collected from activated cells and analyzed for cytokine expression using a Fireplex assay (Abcam). A schematic of the order of addition for this assay is shown in Figure S10.

For monocyte death classification assays, following a 20 min incubation at 37°C, LPS (Invivogen, tlrl-eklps, final assay concentration 1 ng/mL in washing media (WM)) was added and incubated for 3 h at 37°C. ATP (Thermo, R0441; final assay concentration 1mM in WM) or nigericin (Invivogen, tlrl-nig; 20 μM final in WM) was added and incubated for an additional 3 h. Flagellin activation was performed by adding 1 μg/ml Flagellin (final) to cells 20 min after compound addition and incubated for 6 h at 37°C.

Following the activation step, supernatants were harvested for downstream cytokine analysis. Annexin V (AbCam) and SYTOX green (Promega) were added to plates as a measure of cell death and imaged on a Molecular Devices ImageXpress Micro Confocal high content imager (RRID:SCR_020294).

Death classification assays (primary human PBMCs)

Primary human PBMCs were plated, treated with various doses of flagellin (0.625, 1.25, 2.5, 5, 10 μg/mL), staurosporine, digoxin, elesclomol, lanatoside C, darapladib, and doxorubicin (all at 2.5, 5, 10, 20, 40 μM) at 37C for 6 and 24 h, then fixed and stained according to the above plating, fixing, and staining methods with Concanavalin A Alexa Fluor 488 (Thermo C11252) at 25 μg/mL, Phalloidin Phenovue Fluor 568 (PerkinElmer CP25681), and Hoechst 33342 (Thermo). A classifier model was then built on all compounds at all doses and timepoints.

THP1 pyroptosis assay

THP1-HMGB1-Lucia cell line, a commercially available monocyte derived reporter cell line engineered to measure pyroptosis and necrosis via luminescence signal. THP1-HMGB1-Lucia cells were purchased from Invivogen (thp-gb1lc). THP1-HMGB1-Lucia cells were cultured according to manufacturer's instructions and were used at passage 10, 12, or 14, with two freeze thaws – one from purchase and one from banking at passage 6. The second test system was primary human monocytes isolated from healthy human donors and purchased from iXCells.

Inflammasome-mediated pyroptosis was induced via stepwise addition of lipopolysaccharides (LPS) and nigericin. A Microlab Star liquid handler (Hamilton) was used to dilute the prepared compounds in assay media and transferred 20μL of the diluted compounds into an assay plate (Greiner, 781091.) The cells were harvested by pelleting at 300xg for 5 min, manually aspirating supernatant, and resuspending the pellet at 250,000 cells/mL in assay media. 25μls of resuspended cells were transferred to a warmed assay plate using the Microlab Star. During a 20 min preincubation step, an LPS mother plate was prepared with the Microlab Star and 5μL of LPS (Invivogen,tlrl-eklps, final assay concentration 1 μg/mL in assay media) was transferred into the assay plate.The assay plate was shaken at 1000 rpm for 1 min, then incubated for 3 h at 37°. At t = 3h, 5.5μL of nigericin (Invivogen, tlrl-nig, final assay concentration 10μM in assay media) was added to the assay plate with the same automation protocols as the LPS addition. The assay plate was further incubated at 37° for an additional 3 h.

Readouts

High-content widefield fluorescence imaging and image preprocessing

Images were acquired on an ImageXpress Micro Confocal High-Content Imaging System (Molecular Devices) in widefield on a 40× ELWD air objective. Four z-stacks separated by 1μm were acquired and combined using maximum intensity projection, then corrected for illumination. Four fields were collected per well in a 384-well plate using 1x1 binning.

Cytokine expression analysis

Supernatants were collected from the 384-well imaging plates for cytokine analysis. For validation of initial conditions, the FirePlex-HT Human 10-plex Immunoassay (Abcam: ab234897) was run in-house on ImageXPress Micro Confocal (Molecular Devices) microscopes according to the manufacturer's instructions.

For monocyte cell death analysis assays, supernatants were analyzed using nELISA[41] at Nomic Bio.

HMGB1 detection from THP1 reporter cells

QuantiLuc Gold solution was manually prepared according to the manufacturer's instructions and 25μL of the solution was mechanically stamped into a final quantitation plate (Greiner, 655073.) After the 3 h incubation with nigericin, the assay plate was shaken at 1000 rpm for 1 min and centrifuged at 300xg for 1 min 10μL of supernatant was mechanically removed and placed into the quantitation plate, which was manually agitated to mix the solutions. Luminescence, measured at 578 nm and expressed as relative light units (RLUs), was immediately read column-wise at 37C with a Spectramax iD5 plate reader (Molecular Devices).

Computational methods

Extracting visual features as computer vision embeddings

Cell nuclei in each field are localized using a CellProfiler pipeline[21] on the Hoechst-stained images. Square tiles of 82 pixels ("single cell crops") are cropped around the centroid of each nucleus across all stains.

To calculate embeddings, single cell crops are used as input into a convolutional neural network that has been pre-trained on a large number of photographic images and has learned to classify everyday objects within these images. The activations at specific layers are used as black-box features capturing shape and texture properties of the input images. The model architectures and pretrained weights are detailed in the below table.

Convolutional neural networks used to extract visual features from HCI data		
Architecture	Pretrained weights	Embedding layer
VGG16[42]	ImageNet1k	MaxPool of last convolutional layer
EfficientNetV2XL[43]	ImageNet21k	AvgPool of last convolutional layer

The resulting features are high dimensional embeddings, or a list of representative numerical features which have been shown to faithfully represent cellular morphology in an unbiased fashion. When multiple stains are selected, embeddings for each stain are concatenated together to create a single representation.

Morphological profiles

The morphological profile is the well representation obtained by median- (VGG16) or mean- (EfficientNetV2XL) averaging the embeddings of each cell detected in the well. When EfficientNetV2XL embeddings are used, the resulting feature vector is further transformed by computing the top 100 PCA projections with respect to the entire dataset. Finally, each component is z-scored with respect to the activated vehicle distribution for the corresponding donor and plate.

In order to optimize the morphological profiles and understand confounding effects, we executed a set of dedicated experiments publicly released as the Spring Inflammasome Benchmark Dataset (link provided in the key resources table).

We defined a benchmark task where, given a query well and a search pool, the wells in the search pool are ranked by similarity to the query well in the morphological profile space. The mean average precision of finding a technical replicate within the top 20 wells (mAP@20) is the metric used for evaluation. To account for confounding effects, the search pool is defined as all the wells that do not share the plate or donor of the query well.

The benchmark is used to identify the optimal choice of model architecture and pretrained weights for building morphological profiles. The family of EfficientNet-V2 models was considered in virtue of their balance between state-of-the-art accuracy and computational efficiency demonstrated in the context of natural images applications. The below table shows that the best performing model in the Spring Inflammasome Benchmark is the EfficientNet-V2 XL architecture, the largest model in the family, trained on the ImageNet21k dataset. Interestingly, the benchmark score for the other models in the family, which are trained on the smaller ImageNet1k dataset, is inversely correlated with the number of parameters. We hypothesized that, as the model capacity increases, the representations learned become more specific to the domain of the training data.

Comparison of neural networks used to extract visual features from benchmark dataset		
Architecture	Pretrained weights	mAP@20
EfficientNet-V2 B0	ImageNet1k	11.5
EfficientNet-V2 S	ImageNet1k	10.6
EfficientNet-V2 L	ImageNet1k	9.8
EfficientNet-V2 XL	ImageNet21k	13.0

Uniform Manifold Approximation and Projection (UMAP)[24] was used to reduce high dimensional morphological profiles into two unitless dimensions for visualization on a scatterplot.

Phenotypic cell subtype discovery using Ward's method

Hierarchical clustering of VGG16 morphological profiles using Ward's method was used to identify phenotypically distinct cell clusters. Their associations with experimental conditions were determined using odds ratios, and a Bonferroni corrected Fisher's exact test was used to calculate p-value (0.01 threshold for significance).

Median number of cells per well belonging to a cluster were used to determine compound mediated effects. Median values were averaged across replicates and normalized as a fraction of the average median of vehicle control replicates.

Compound mediated distribution shift (CMDS) of morphological profiles

The CMDS scoring is complementary to the targeted strategy because it does not rely on specific control inhibitors as reference. It is based on the following postulate: morphological profiles of non-toxic, ASC speck suppressing compounds that deviate significantly from the activated vehicle control distribution must correspond to an inhibition mechanism along the specific inflammasome pathway. The CMDS approach enables discovery and mechanistic classification of compounds that don't share commonalities with known control inhibitors.

Given that morphological profiles were z-scored against activated vehicle control distribution for the corresponding donor, plate and activator, the individual vector components of activated vehicle control profiles are normally distributed. The Euclidean norm of a profile vector represents the overall distance from the average activated vehicle control profile.

Four quadrants were defined in the morphological profile norm plane using the 99-th percentiles of the activated vehicle distribution for ATP or flagellin as thresholds. Compounds that mediate shifts above the threshold for both activation states are called late stage inhibitors, while those with single condition effects are called early or pathway specific inhibitors. For each control inhibitor the

fraction of replicas beyond the 95-th percentile of the activated vehicle distribution is reported alongside the average *p*-value obtained by comparing 2 randomly sampled replicas against the activated vehicle distribution (null hypothesis) using Welch's t-test.

Compounds meeting these thresholds are those that induce measurable effects on activated cells, so to filter for compounds that induce inflammasome relevant responses, we filtered out compounds with high toxicity scores or that do not induce a change in ASC specks.

Ranking software tool feature quantifications and scoring

Single cell quantifications were aggregated on a per well basis and median values were analyzed using statsmodels.regression.linear_model.OLS. Here, an ordinary least-squares regression model is applied to the data to extract mean differences, *p*-values, and confidence intervals relative to the activated donor control. Calculated values for each feature for every compound treatment are then ingested into our data organization and visualization software.

For scoring purposes, we first assigned fixed quantities to *p*-values (calculated using two-tailed t-tests) according to their confidence levels (*p*-value $<0.05 = 0.5$; *p*-value $<0.01 = 1$). This heuristic was applied to ensure features are standardized and directly comparable. Those values were then multiplied by directional weights (-10 to $+10$) for the features selected for a given individual score, as detailed in Figure S4A (screening data) or Figure S7B (multi-activator data). Individual scores were generated as a weighted sum of the selected features.

Individual scores for screening data were designed as follows: four individual scores were used to analyze screening data. Briefly, the scores were generated using the following criteria (detailed in Figure S4A): (1) general (increase clusters 1 and 2, decrease cluster 3, decrease ASC specks, increase ASC speck area), (2) early pathway (decrease in off-basis, increase in on-basis, similarity to A-804598 (ATP only)), (3) terminal pathway (similarity to disulfiram, increase cluster 4), and (4) toxicity (decrease cluster 1, increase % dying T cells, increase % damaged nuclei, increase % dying macrophages, and decrease in % monocytes).

Aggregated scores for screening data were applied as follows: Boolean operators were used to classify compounds from screening data into four mechanistic classes based on their individual score performance as follows: early class (general plus early scores combined >75, terminal scores <10, relative ATP::Flagellin relationship [(Max-Min)/Max] of <0.6), convergent class (general scores + early ATP scores >40, general + early Flagellin scores >50, and terminal scores <10 for both activation conditions), terminal class (general scores >5 for both conditions, and terminal scores >10 for both conditions).

Stringent TSCC for visualizations in figures: Early: >120 (sum of general + early per condition) for one condition and a relative ATP::Flagellin relationship [(Max-Min/Max)] of ≥ 0.7; Terminal: general >15, terminal >10 for both ATP and flagellin; Convergent: early scores >60 for ATP and >90 for flagellin, with relative ATP::Flagellin relationship [(Max-Min/Max)] of <0.7.

Individual scores for multi-activator data were designed as follows: seven individual scores were applied to multi-activator data and detailed in Figure S7B. The scores were generated using the following criteria for every compound for each of the six conditions: (1) general inhibitor score (decrease ASC speck presence, increase in clusters 1 and 2, decrease in cluster 3), (2) early pathway score (ATP condition: increase in similarity to A-804598, decrease in similarity to activated ATP; flagellin condition: decrease in similarity to activated flagellin), (3) MCC950 similarity (increase in similarity to MCC950), (4) late/GSDMD pathway (increase in similarity to disulfiram, increase in cluster 4), (5) Convergence (decrease in cluster 4, increase in similarity to TH1020), (6) on basis (increase), (7) off basis (increase). A pathway multiplier (the sum of conditions with positive general scores) was also calculated for each compound.

Aggregated scores for multi-activator data were applied as follows: five aggregate scores for compound classification of multi-activator data were designed using insights from hierarchical clustering of *Z* score normalized individual scoring data using Ward's method. Compounds were assigned to mechanistic classes according to their respective maximum aggregate scores.

The five scoring rubrics were calculated as follows and described in Figure S7C:

Early pathway scores were used to assign compounds into Early ATP, Early Flagellin, or Early Convergent classes, and were calculated as the weighted sum of the individual on-basis and early pathway scores. *Class 1:* For early ATP designation, ATP early pathway score was penalized by half if the pathway multiplier exceeded 3, and the resulting value must be > 2.5x flagellin early pathway score to be considered for this class. *Class 2:* Early flagellin pathway designation used the same strategy as early ATP, but with the flagellin early pathway score. *Class 3:* Early convergence score was determined by a sum of the convergence multiplier with the positive z-scored values for each condition, and divided by the total number of conditions. *Class 4:* The late convergence pathway score was a weighted sum of the convergence score and MCC950 similarity score, minus the Late/gasdermin D score for each condition. Positive *Z* score normalized values for each condition were added with the convergence multiplier and divided by the total number of conditions. *Class 5:* The Terminal aggregate score was a weighted sum of Late/gasdermin D score and high off-basis, minus the convergence score for each condition. Positive *Z* score normalized values for each condition were added with the convergence multiplier and divided by the total number of conditions. All scoring was executed in Microsoft Excel.

Classification models

Classification models were trained on the VGG16 morphological profiles of each well using XGBoost,[44] an implementation of gradient-boosted decision trees. All results are reported using a 4-fold cross-validation, whereby each fold is defined by training on 16 donors, and testing on 8 unseen donors.

Prediction of activator or inhibitor signatures is determined by applying trained classifiers to images of compound treated cells. This feature is measured on a 0–1 scale, with 0 indicating the lowest observed value, and 1 indicating the highest observed value.

Projection scores

On- and off-basis scores were generated from the same VGG16 morphological profiles used for the classifiers. A basis vector for each activation condition is first established in the embedding space; this vector leads from an activated vehicle control condition to the corresponding basal vehicle control condition on the same plate. Replicates of the activated and basal wells are first median-aggregated to generate a single profile prior to the creation of the basis vector.

On-basis scores are calculated by generating a vector from the activated-vehicle controls to individual compounds, and then taking its normalized scalar projection onto the basis vector for the given activated vehicle-control. The output is a singular, scalar value, where 1.0 represents the basal state and 0.0 represents the activated state. Off-basis scores are similarly calculated, but with a normalized scalar rejection and an a singular, scalar output value, where large values represent phenotypic differences that are comparable or greater than the differences between the basal and activated states, and 0.0 means a compound does not induce orthogonal phenotypic differences.

Automated measurement of ASC specks (presence, area, distribution, and distance)

Using the ASC imaging channel, a set of ground-truth labels were built classifying cells as ASC positive or negative. Then, an algorithm was trained on the example set using embeddings + XGBoost to recognize ASC speck positivity. Image filters were applied to ASC speck positive samples to binarize the ASC channel for speck detection. The measure.regionprops method from the scikit-image Python package[45] was then used to measure the location and size of ASC specks.

The ASC presence measurement is the median number of cells per well detected with an ASC speck (binary scale where 1 is present, 0 is absent). ASC area is the average area (μM) of detected specks in a well, cellular overlap determines if a speck is detected within or external to the cell (0 is external, 1 is internal), and nuclear or cellular distance is the length from the nuclear or cellular center (μM).

Monocytic death classification analysis

Using Annexin V and Sytox Green imaging channels, an example set was built by assigning 100 example cells into three classes: (1) healthy/alive (Annexin V^- SYTOX green$^-$ cells), (2) apoptotic (Annexin V^+ SYTOX green$^-$), and (3) pyroptotic (Annexin V^+ SYTOX green$^+$). Then, an algorithm was trained on the example set using embeddings + XGBoost to recognize these classes.

QUANTIFICATION AND STATISTICAL ANALYSIS

Titration curves and IC50 determination

Inhibition curves were fit using a log(agonist) vs. response variable slope (four parameters) least squares fit model using GraphPad Prism software package (RRID:SCR_002798). IC50s were calculated from these curves using Prism software.

THP1 assay

relative luminescence unit values (RLUs) were plotted against the log of disulfiram concentrations using GraphPad Prism software. Details of number of replicates per experiment and number of experiments are detailed in the figure legends.

IL-1β expression

For representative experimental data, average pg/ml of replicates was plotted against the log of the compound concentrations using GraphPad Prism software. For analysis of multiple experiments, average pg/ml of replicates was normalized as the percentage of activated vehicle control (DMSO). Details of number of replicates per experiment and number of experiments are detailed in the figure legends.

Monocytic cell death analyses

Pyroptosis, alive, and apoptosis calculations were performed for each compound treatment by calculating the fraction of the activated or basal vehicle control (value of condition replicate/average value control replicates). Details of number of replicates per experiment and number of experiments are detailed in the figure legends.

Statistical significance between groups

Statistical significance between groups was determined using unpaired Mann Whitney u-tests with a 1% false discovery rate to correct for multiple comparisons, with a significance threshold of $p < 0.05$. Details of number of replicates per experiment and number of experiments are detailed in the figure legends.

Principal component analysis (PCA)

GraphPad Prism was used to perform PCA on the correlation matrix (standardized) of z-scored aggregate scores from the multi-activator PBMC data. According to GraphPad Prism software, PCs were selected using parallel analysis, which performs Monte Carlo simulations on random data of equal dimension to the input data, and calculates eigenvalues for resulting PCs. PCs with eigenvalues greater than 95% of the 1000 simulations were selected.

PCA of death classification monocyte data were similarly performed on compound data normalized as a percentage of alive (activated), alive (basal), or pyroptotic activated controls. Score plots are shown as scatterplots of the first two principal components, with each point representing the data for a single compound, as indicated in the figure legends.

Statistical measurements from computational analyses

Statistics used for computational analyses are described in the method details text and figure legends.